

An Open-Source Pseudo-Spectral Solver for Idealized Korteweg–de Vries Soliton Simulations

Dasapta Erwin Irawan^{1,*}, Sandy Hardian Susanto Herho^{2,3,4,5}, Astyka Pamumpuni¹,
Rendy Dwi Kartiko¹, Faruq Khadami⁶, Iwan Pramesti Anwar⁶,
Karina Aprilia Sujatmiko⁶, Alfita Puspa Handayani^{5,7},
Faiz Rohman Fajary⁸, and Rusmawan Suwarman⁸

¹Applied Geology Research Group, Bandung Institute of Technology, Bandung, West Java 40132, Indonesia

²Department of Earth and Planetary Sciences, University of California, Riverside, CA 92521, USA

³Ronin Institute for Independent Scholarship 2.0, Sacramento, CA 95816, USA

⁴School of Systems Science and Industrial Engineering, State University of New York, Binghamton, NY 13902, USA

⁵Center for Agrarian Studies, Bandung Institute of Technology, Bandung, West Java 40132, Indonesia

⁶Applied and Environmental Oceanography Research Group, Bandung Institute of Technology, Bandung, West Java 40132, Indonesia

⁷Spatial Systems and Cadaster Research Group, Bandung Institute of Technology, Bandung, West Java 40132, Indonesia

⁸Atmospheric Science Research Group, Bandung Institute of Technology, Bandung, West Java 40132, Indonesia

*Correspondence: dasaptaerwin@itb.ac.id

Abstract

The Korteweg–de Vries (KdV) equation is a foundational model in geophysical fluid dynamics (GFD), governing the propagation of long internal and surface gravity waves in stratified and shallow ocean environments where the interplay between nonlinear steepening and frequency-dependent dispersion gives rise to solitons. Although the analytical tractability of the KdV equation through inverse scattering is well established, systematic numerical exploration of multi-soliton interactions remains valuable for benchmarking solvers, probing conservation properties under varied oceanic initial conditions, and building intuition for more complex ocean wave phenomena. This article presents **sangkuriang**, an open-source Python library that solves the KdV equation using Fourier pseudo-spectral spatial discretization and adaptive eighth-order Runge–Kutta time integration. The implementation leverages just-in-time (JIT) compilation to achieve research-grade computational efficiency on standard hardware. The solver is validated through four progressively complex idealized scenarios motivated by oceanic wave dynamics: isolated soliton propagation, symmetric interactions, overtaking collisions, and three-body interactions. High-fidelity conservation of mass, momentum, and energy is demonstrated, with relative errors remaining below $\mathcal{O}(10^{-4})$ across all test cases. Measured soliton velocities align with theoretical predictions within 5%, confirming the capture of the amplitude-dependent dispersion characteristic of oceanic solitary waves. Complementary diagnostics, including spectral entropy and recurrence quantification analysis (RQA), verify that the numerical solutions preserve the regular phase-space structure characteristic of integrable Hamiltonian systems. These results establish **sangkuriang** as a robust, lightweight platform for reproducible numerical investigation of idealized nonlinear dispersive wave dynamics relevant to coastal and ocean engineering applications.

Keywords: Korteweg–de Vries equation; pseudo-spectral methods; soliton dynamics; nonlinear ocean waves; shallow water waves

1 Introduction

The Korteweg–de Vries (KdV) equation occupies a central position in geophysical fluid dynamics (GFD) as the prototypical completely integrable partial differential equation (PDE) admitting soliton solutions [1]. Originally derived to describe long gravity waves in shallow channels [2], the equation demonstrates how competing nonlinear steepening and linear dispersion can balance to produce localized, shape-preserving pulses—solitons—that survive mutual collisions with only phase shifts [3]. The discovery that this behavior is rooted in complete integrability, with an infinite hierarchy of conservation laws accessible through inverse scattering [4, 5], elevated the KdV equation to a cornerstone of mathematical physics, with applications spanning plasma dynamics, internal ocean waves, and condensed matter systems [6].

In the oceanic context, the KdV framework and its extensions have proven indispensable for describing nonlinear internal solitary waves (ISWs), which are among the most energetic high-frequency phenomena in the coastal and deep ocean [46, 47]. Satellite imagery and in situ observations have documented large-amplitude ISWs in numerous marginal seas, including the South China Sea, the Andaman Sea [49], and the Sulu Sea, where these waves modulate acoustic propagation, drive turbulent mixing, and exert forces on offshore structures [48]. While realistic ocean modeling requires variable-coefficient and higher-order extensions of the KdV equation [48, 50], the constant-coefficient idealization retains its importance as the canonical benchmark for understanding the fundamental balance between nonlinearity and dispersion that underpins oceanic solitary wave dynamics [6, 46].

Although the analytical structure of soliton theory is well established, numerical simulation remains indispensable for exploring parameter regimes, validating approximate initial conditions, and characterizing transient interaction dynamics that resist closed-form description [7]. In particular, the quantitative assessment of conservation law preservation, amplitude-dependent dispersion, and phase-space regularity across multi-soliton configurations requires flexible computational tools capable of high-fidelity integration over extended time intervals [8]. Such capabilities are especially relevant to idealized studies of oceanic internal wave interactions, where multi-soliton collisions and overtaking events are routinely observed in field campaigns [51].

Python has become a widely adopted language for scientific computing in the geosciences and oceanography, owing to its extensive numerical ecosystem and low overhead for prototyping [9, 10]. Libraries such as NumPy and SciPy [11, 12] provide efficient implementations of core algorithms—fast Fourier transforms (FFT), adaptive ODE solvers, and dense linear algebra—while just-in-time (JIT) compilation via Numba [13] bridges the gap between interpreted flexibility and compiled performance [14]. These capabilities have made Python increasingly viable for production-level numerical experiments in computational geophysics [15, 16].

Pseudo-spectral methods are particularly well suited to the KdV equation. By representing spatial derivatives as multiplications in wavenumber space, Fourier-based discretizations achieve exponential convergence for smooth periodic solutions while naturally respecting the spectral structure of dispersive operators [17, 18]. This approach has a long and successful history in the numerical treatment of nonlinear dispersive PDEs arising in ocean wave theory [19, 20].

In this work, we present `sangkuriang`, an open-source Python library for solving the KdV equation using Fourier pseudo-spectral spatial discretization coupled with adaptive eighth-order Runge–Kutta time integration via the Dormand–Prince 8(5,3) (DOP853) method [21, 22]. Performance-critical routines are accelerated through Numba JIT compilation with multi-core parallelization, enabling research-grade simulations on commodity hardware. The library provides both a command-line interface for rapid deployment with predefined test cases and a Python API for programmatic access. Simulation data are output in Network Common Data Format (NetCDF) following Climate and Forecast (CF) conventions [23], ensuring interoperability with standard oceanographic and geoscientific analysis workflows. The solver additionally incorporates diagnostic routines for monitoring conservation laws, tracking soliton trajectories, and generating animated visualizations. The software is freely available from the Python Package Index (PyPI) under a permissive open-source license.

We revisit the classical benchmarks of KdV soliton dynamics—single-soliton propagation, symmetric two-soliton configurations, overtaking collisions, and three-body interactions—framed as idealized analogs of oceanic solitary wave phenomena, with an emphasis on quantitative diagnostics that go beyond visual inspection. Specifically, we employ information-theoretic measures (spectral entropy, LMC statistical complexity, Fisher information) and recurrence quantification analysis to characterize the phase-space structure of the computed solutions. These complementary diagnostics provide model-independent evidence for the preservation of integrability under numerical integration and offer tools that may prove useful in studying perturbed or extended KdV-type systems relevant to realistic ocean stratification and bathymetric variability, where analytical guarantees are unavailable.

2 Materials and Methods

2.1 Model Description

The KdV equation constitutes one of the most fundamental nonlinear PDEs in GFD, governing the propagation of weakly nonlinear, weakly dispersive long waves in shallow ocean basins, coastal shelves, and stratified water columns [2, 3]. The derivation presented here proceeds from first principles beginning with the three-dimensional Euler equations for an inviscid ocean layer, following the established asymptotic analysis framework employed in ocean wave theory [7, 6].

Consider an inviscid, incompressible fluid occupying a domain bounded below by a rigid horizontal seabed at $z = 0$ and above by a free surface at $z = h_0 + \eta(x, y, t)$, where h_0 denotes the undisturbed water depth and η represents the free surface displacement (Figure 1). The fluid is subject to gravitational acceleration g acting in the negative z -direction. This configuration represents an idealized coastal or continental shelf environment in which long surface gravity waves propagate over a flat bottom—a standard starting point for shallow water wave theory in physical oceanography [24, 46].

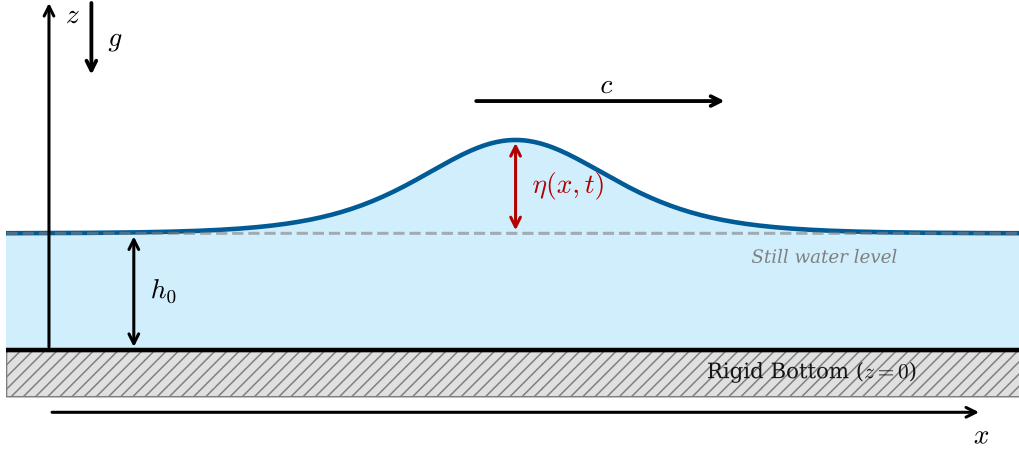


Figure 1: Schematic of the shallow ocean wave domain. The fluid occupies a region bounded below by a rigid horizontal seabed at $z = 0$ and above by a free surface at $z = h_0 + \eta(x, t)$, where h_0 denotes the undisturbed water depth and $\eta(x, t)$ represents the free surface displacement. Gravitational acceleration g acts in the negative z -direction, and wave propagation occurs along the x -axis with phase speed c .

For an inviscid fluid, the three-dimensional incompressible Euler equations governing the velocity field $\mathbf{u} = (u, v, w)$ and pressure p read

$$\nabla \cdot \mathbf{u} = \frac{\partial u}{\partial x} + \frac{\partial v}{\partial y} + \frac{\partial w}{\partial z} = 0, \quad (1)$$

$$\frac{\partial u}{\partial t} + u \frac{\partial u}{\partial x} + v \frac{\partial u}{\partial y} + w \frac{\partial u}{\partial z} = -\frac{1}{\rho} \frac{\partial p}{\partial x}, \quad (2)$$

$$\frac{\partial v}{\partial t} + u \frac{\partial v}{\partial x} + v \frac{\partial v}{\partial y} + w \frac{\partial v}{\partial z} = -\frac{1}{\rho} \frac{\partial p}{\partial y}, \quad (3)$$

$$\frac{\partial w}{\partial t} + u \frac{\partial w}{\partial x} + v \frac{\partial w}{\partial y} + w \frac{\partial w}{\partial z} = -\frac{1}{\rho} \frac{\partial p}{\partial z} - g, \quad (4)$$

where ρ is the constant fluid density. These equations are supplemented by boundary conditions at the seabed and free surface [24, 25].

At the rigid seabed $z = 0$, the impermeability condition requires

$$w = 0 \quad \text{at} \quad z = 0. \quad (5)$$

At the free surface $z = h_0 + \eta(x, y, t)$, the kinematic boundary condition states that fluid particles on the surface remain on the surface:

$$w = \frac{\partial \eta}{\partial t} + u \frac{\partial \eta}{\partial x} + v \frac{\partial \eta}{\partial y} \quad \text{at} \quad z = h_0 + \eta, \quad (6)$$

and the dynamic boundary condition requires continuity of normal stress, which for an inviscid fluid with negligible surface tension reduces to

$$p = p_{\text{atm}} \quad \text{at} \quad z = h_0 + \eta, \quad (7)$$

where p_{atm} is the constant atmospheric pressure.

We now restrict attention to unidirectional wave propagation along the x -axis, setting $v = 0$ and $\partial/\partial y = 0$. This reduction is appropriate for long-crested ocean waves propagating shoreward over a continental shelf or along a waveguide [47]. The governing equations (1)–(4) reduce to the two-dimensional system

$$\frac{\partial u}{\partial x} + \frac{\partial w}{\partial z} = 0, \quad (8)$$

$$\frac{\partial u}{\partial t} + u \frac{\partial u}{\partial x} + w \frac{\partial u}{\partial z} = -\frac{1}{\rho} \frac{\partial p}{\partial x}, \quad (9)$$

$$\frac{\partial w}{\partial t} + u \frac{\partial w}{\partial x} + w \frac{\partial w}{\partial z} = -\frac{1}{\rho} \frac{\partial p}{\partial z} - g. \quad (10)$$

To derive the shallow water equations, we introduce characteristic scales: λ for horizontal length (the dominant wavelength), h_0 for vertical length (the water depth), a for wave amplitude, λ/c_0 for time (where $c_0 = \sqrt{gh_0}$ is the linear long-wave speed), c_0 for horizontal velocity, and ρgh_0 for pressure. The dimensionless variables are defined as

$$\tilde{x} = \frac{x}{\lambda}, \quad \tilde{z} = \frac{z}{h_0}, \quad \tilde{t} = \frac{c_0 t}{\lambda}, \quad \tilde{\eta} = \frac{\eta}{a}, \quad \tilde{u} = \frac{u}{c_0}, \quad \tilde{w} = \frac{w \lambda}{c_0 h_0}, \quad \tilde{p} = \frac{p - p_{\text{atm}}}{\rho g h_0}. \quad (11)$$

Two fundamental small parameters emerge naturally: the amplitude parameter $\alpha = a/h_0 \ll 1$ measuring wave nonlinearity, and the dispersion parameter $\beta = (h_0/\lambda)^2 \ll 1$ quantifying the shallowness of the water [26]. In typical continental shelf settings where long gravity waves or internal solitary waves are observed, both α and β are indeed small, placing the dynamics squarely within the weakly nonlinear, weakly dispersive regime that the KdV equation governs [46, 48].

Substituting the scalings (11) into equations (8)–(10) and dropping tildes for clarity, we obtain the dimensionless system

$$\frac{\partial u}{\partial x} + \frac{\partial w}{\partial z} = 0, \quad (12)$$

$$\frac{\partial u}{\partial t} + \alpha \left(u \frac{\partial u}{\partial x} + w \frac{\partial u}{\partial z} \right) = -\frac{\partial p}{\partial x}, \quad (13)$$

$$\beta \left[\frac{\partial w}{\partial t} + \alpha \left(u \frac{\partial w}{\partial x} + w \frac{\partial w}{\partial z} \right) \right] = -\frac{\partial p}{\partial z} - 1. \quad (14)$$

The factor β multiplying the left-hand side of equation (14) indicates that vertical accelerations are negligible in the shallow water limit $\beta \rightarrow 0$, consistent with the hydrostatic approximation widely employed in large-scale ocean circulation models [27].

In the leading-order shallow water approximation ($\beta = 0$), equation (14) reduces to the hydrostatic balance

$$\frac{\partial p}{\partial z} = -1, \quad (15)$$

which, upon integration from z to the free surface $z = 1 + \alpha\eta$ using the dynamic boundary condition $p = 0$ at $z = 1 + \alpha\eta$, yields

$$p = 1 + \alpha\eta - z. \quad (16)$$

Thus, the horizontal pressure gradient becomes

$$\frac{\partial p}{\partial x} = \alpha \frac{\partial \eta}{\partial x}, \quad (17)$$

independent of z , implying that the horizontal velocity u is also independent of depth at leading order.

Integrating the continuity equation (12) from $z = 0$ to $z = 1 + \alpha\eta$ and applying the boundary conditions (5) and (6), we obtain

$$\frac{\partial \eta}{\partial t} + \frac{\partial}{\partial x} [(1 + \alpha\eta)u] = 0. \quad (18)$$

Combining with the horizontal momentum equation (13) and pressure gradient (17), we arrive at the nonlinear shallow water equations in dimensionless form [24]

$$\frac{\partial \eta}{\partial t} + \frac{\partial}{\partial x} [(1 + \alpha\eta)u] = 0, \quad (19)$$

$$\frac{\partial u}{\partial t} + \alpha u \frac{\partial u}{\partial x} + \frac{\partial \eta}{\partial x} = 0. \quad (20)$$

These equations are exact within the hydrostatic shallow water approximation but remain coupled and nonlinear. They form the basis of many operational coastal and tsunami models, but lack the dispersive corrections necessary to sustain solitary wave solutions [50].

To incorporate weak dispersion and derive the KdV equation, we retain terms of order β in the vertical momentum equation (14). The regime $\alpha \sim \beta \sim \mathcal{O}(\delta) \ll 1$ with δ representing a single small parameter defines the Boussinesq scaling, wherein nonlinear and dispersive effects balance to produce solitary wave solutions [26]. This balance is the essential physical mechanism underlying the formation of internal solitary waves observed in shelf-slope regions worldwide [46, 49]. Under this scaling, we seek asymptotic solutions in the form of perturbation expansions

$$\eta(\xi, \tau) = \delta\eta_1(\xi, \tau) + \delta^2\eta_2(\xi, \tau) + \mathcal{O}(\delta^3), \quad (21)$$

$$u(\xi, \tau) = \delta u_1(\xi, \tau) + \delta^2 u_2(\xi, \tau) + \mathcal{O}(\delta^3), \quad (22)$$

where $\delta = \sqrt{\alpha} = \sqrt{\beta}$ serves as the expansion parameter. Substituting expansions (21) and (22) into the shallow water equations and collecting terms of equal powers in δ , we obtain at leading order $\mathcal{O}(\delta)$ the linearized wave equations

$$\frac{\partial \eta_1}{\partial \tau} + \frac{\partial u_1}{\partial \xi} = 0, \quad (23)$$

$$\frac{\partial u_1}{\partial \tau} + \frac{\partial \eta_1}{\partial \xi} = 0. \quad (24)$$

These admit right-going wave solutions of the form $\eta_1 = f(\xi - \tau)$ and $u_1 = f(\xi - \tau)$, where f is an arbitrary waveform propagating with dimensionless speed unity (dimensional speed $c_0 = \sqrt{gh_0}$).

At the next order $\mathcal{O}(\delta^2)$, nonlinear and dispersive corrections emerge [1]:

$$\frac{\partial \eta_2}{\partial \tau} + \frac{\partial u_2}{\partial \xi} = -\frac{\partial}{\partial \xi} (\eta_1 u_1), \quad (25)$$

$$\frac{\partial u_2}{\partial \tau} + \frac{\partial \eta_2}{\partial \xi} = -u_1 \frac{\partial u_1}{\partial \xi} + \frac{1}{3} \frac{\partial^3 u_1}{\partial \xi^2 \partial \tau}. \quad (26)$$

The nonlinear term $-\partial_\xi(\eta_1 u_1)$ in equation (25) arises from the advection of mass by the wave motion, while the dispersive term $\frac{1}{3} \partial_\xi^2 \partial_\tau u_1$ in equation (26) originates from the vertical acceleration induced by the sloping bottom pressure distribution [27].

To eliminate secular growth and derive a consistent evolution equation, we introduce the stretched slow variables $X = \delta(\xi - \tau)$ and $T = \delta^2 \tau$, representing a coordinate system moving with the linear wave speed and a slow time scale appropriate for observing cumulative nonlinear and dispersive effects [6]. We seek solutions in the form $\eta_1 = U(X, T)$ and apply the multiple scales method. The chain rule yields

$$\frac{\partial}{\partial \xi} = \delta \frac{\partial}{\partial X}, \quad \frac{\partial}{\partial \tau} = -\delta \frac{\partial}{\partial X} + \delta^2 \frac{\partial}{\partial T}. \quad (27)$$

Combining the solvability conditions at order $\mathcal{O}(\delta^3)$ to suppress resonant secular terms, and transforming back to dimensional variables through the scalings $x = \lambda X$, $t = \lambda T \sqrt{h_0/g}$, and $\eta = aU$, we obtain the canonical KdV equation in dimensional form [7]

$$\frac{\partial \eta}{\partial t} + c_0 \frac{\partial \eta}{\partial x} + \frac{3c_0}{2h_0} \eta \frac{\partial \eta}{\partial x} + \frac{c_0 h_0^2}{6} \frac{\partial^3 \eta}{\partial x^3} = 0, \quad (28)$$

where $c_0 = \sqrt{gh_0}$ denotes the linear shallow water wave speed. This formulation makes explicit the physical origins of each term: the second term represents linear wave propagation at the long-wave phase speed, the third term captures amplitude-dependent steepening (nonlinearity) responsible for wave breaking in the absence of dispersion, and the fourth term describes frequency-dependent dispersion that spreads energy across wavenumbers. The competition between these last two effects is the fundamental mechanism sustaining solitary waves in shallow ocean environments [46, 48].

For computational implementation and to emphasize the balance between nonlinearity and dispersion, we transform equation (28) to a traveling coordinate frame $\chi = x - c_0 t$ and define $u(\chi, t) = \eta(x, t)$. Furthermore, we introduce dimensionless parameters $\varepsilon = 3c_0/(2h_0)$ [m⁻¹] characterizing the nonlinearity strength and $\mu = c_0 h_0^2/6$ [m³/s] quantifying dispersion. This yields the standard form employed in the numerical solver [17, 20]

$$\frac{\partial u}{\partial t} + \varepsilon u \frac{\partial u}{\partial x} + \mu \frac{\partial^3 u}{\partial x^3} = 0, \quad (29)$$

where we have relabeled $\chi \rightarrow x$ for notational simplicity. In equation (29), $u(x, t)$ represents the wave amplitude field [m], with spatial coordinate x [m] and temporal coordinate t [s]. The remarkable property of this equation lies in the exact balance between the quadratic nonlinear term $\varepsilon u \partial_x u$, which steepens wave profiles and would induce shock formation in isolation, and the third-order dispersive term $\mu \partial_x^3 u$, which spreads energy and favors shorter wavelengths. When these mechanisms achieve equilibrium, the equation admits solitary wave solutions—solitons—that propagate without change of form [3]. This idealized balance captures the essential physics of long nonlinear waves observed on continental shelves, in straits, and in the thermocline of the open ocean [47, 51].

The KdV equation (29) possesses profound mathematical structure as a completely integrable Hamiltonian system. It admits an infinite hierarchy of conservation laws, the first three of which correspond to physically meaningful quantities [28, 4]. The mass functional

$$M[u] = \int_{-\infty}^{\infty} u(x, t) dx \quad (30)$$

represents the total wave amplitude integrated over space, analogous to volume conservation in the ocean surface layer. The momentum functional

$$P[u] = \int_{-\infty}^{\infty} u^2(x, t) dx \quad (31)$$

corresponds to the square-integrated field, related to wave action in the physical system. The energy functional

$$E[u] = \int_{-\infty}^{\infty} \left[\frac{\varepsilon}{2} u^3 - \frac{3\mu}{2} \left(\frac{\partial u}{\partial x} \right)^2 \right] dx \quad (32)$$

represents the Hamiltonian of the system, with the cubic term $\frac{\varepsilon}{2} u^3$ encoding nonlinear potential energy and the quadratic gradient term $-\frac{3\mu}{2} (\partial_x u)^2$ representing dispersive kinetic energy. These invariants (30)–(32) satisfy $dM/dt = 0$, $dP/dt = 0$, and $dE/dt = 0$ along solutions of equation (29), providing essential diagnostics for numerical accuracy [6]. Their preservation under numerical integration is a necessary condition for any solver intended to reproduce the long-time dynamics of oceanic solitary waves faithfully.

The KdV equation (29) admits exact single-soliton solutions in the form [1]

$$u(x, t) = \frac{A}{\cosh^2 \left[\sqrt{\frac{\varepsilon A}{12\mu}} (x - x_0 - vt) \right]}, \quad (33)$$

where $A > 0$ denotes the soliton amplitude [m], x_0 represents the initial position [m], and the propagation velocity

[m/s] is given by

$$v = \frac{\varepsilon A}{3}. \quad (34)$$

Equation (34) reveals the fundamental nonlinear dispersion relation: taller solitons travel faster, enabling overtaking collisions. This amplitude–velocity relationship is a robust feature of oceanic internal solitary waves, where larger-amplitude ISWs are consistently observed to propagate faster than their smaller counterparts [46, 49]. The width parameter $w = \sqrt{12\mu/(\varepsilon A)}$ [m] characterizes the spatial extent, demonstrating that larger amplitudes produce narrower, faster solitons—a relationship well documented in field observations of ISWs on continental shelves [48]. The remarkable stability of these solutions under mutual collisions—emerging unchanged except for phase shifts—constitutes the defining characteristic of soliton behavior and validates the KdV equation as an integrable system [3, 5].

2.2 Numerical Implementation

The numerical solution of the KdV equation (29) requires spatial discretization of the differential operators and temporal integration of the resulting semi-discrete system. The `sangkuriang` solver employs the Fourier pseudo-spectral method for spatial derivatives [18, 19], which may provide exponential convergence rates for smooth periodic solutions, combined with adaptive high-order explicit time integration. This approach has been demonstrated to be effective for nonlinear dispersive wave equations arising in ocean and atmospheric dynamics [17, 8].

Consider a periodic spatial domain $x \in [x_{\min}, x_{\max}]$ with length $L = x_{\max} - x_{\min}$. We discretize this domain using N uniformly spaced grid points $x_j = x_{\min} + j\Delta x$ for $j = 0, 1, \dots, N-1$, where the spatial resolution is $\Delta x = L/N$. Let $u_j(t) = u(x_j, t)$ denote the semi-discrete solution at grid point x_j and time t . The periodicity condition $u(x_{\min}, t) = u(x_{\max}, t)$ is implicitly enforced through the DFT representation. While ocean domains are not strictly periodic, the periodic boundary assumption is standard in idealized KdV studies and is justified when soliton amplitudes decay sufficiently before reaching the domain boundaries [17, 20]. The DFT and its inverse are defined as [29]

$$\hat{u}_k = \frac{1}{N} \sum_{j=0}^{N-1} u_j \exp\left(-\frac{2\pi i k j}{N}\right), \quad k = 0, 1, \dots, N-1, \quad (35)$$

$$u_j = \sum_{k=0}^{N-1} \hat{u}_k \exp\left(\frac{2\pi i k j}{N}\right), \quad j = 0, 1, \dots, N-1, \quad (36)$$

where \hat{u}_k represents the k -th Fourier coefficient and $i = \sqrt{-1}$ denotes the imaginary unit. The computational implementation utilizes the FFT algorithm [30] available in NumPy [11], reducing the operation count from $\mathcal{O}(N^2)$ to $\mathcal{O}(N \log N)$ for both forward and inverse transforms.

The wavenumber vector corresponding to the DFT basis functions is given by

$$k_n = \begin{cases} \frac{2\pi n}{L}, & n = 0, 1, \dots, \lfloor N/2 \rfloor, \\ \frac{2\pi(n-N)}{L}, & n = \lceil N/2 \rceil, \dots, N-1, \end{cases} \quad (37)$$

where the convention in equation (37) accounts for the standard FFT frequency ordering, with negative frequencies wrapped to the upper half of the index range. This wavenumber array can be efficiently generated using `numpy.fft.fftfreq` [11]. The spectral derivative operator acts on the Fourier coefficients through multiplication by ik_n . For the first-order spatial derivative, we have

$$\frac{\partial u}{\partial x}(x_j) = \text{IFFT}[ik_n \cdot \text{FFT}[u_j]] = \text{IFFT}[ik_n \hat{u}_k], \quad (38)$$

where $\text{FFT}[\cdot]$ and $\text{IFFT}[\cdot]$ denote the DFT (35) and its inverse (36), respectively. The third-order derivative required for the dispersion term follows analogously:

$$\frac{\partial^3 u}{\partial x^3}(x_j) = \text{IFFT}[(ik_n)^3 \hat{u}_k]. \quad (39)$$

The real part of the inverse transform is extracted to eliminate numerical round-off errors in the imaginary component, which should theoretically vanish for real-valued solutions. This spectral differentiation approach is exact in the continuous limit and introduces errors only through aliasing in the nonlinear term, which can be controlled through sufficient spatial resolution [31].

Applying the spatial discretization described by equations (38) and (39) to the KdV equation (29), we obtain the semi-discrete ordinary differential equation (ODE) system

$$\frac{du_j}{dt} = F_j(\mathbf{u}(t)), \quad j = 0, 1, \dots, N-1, \quad (40)$$

where $\mathbf{u}(t) = [u_0(t), u_1(t), \dots, u_{N-1}(t)]^T \in \mathbb{R}^N$ denotes the state vector and the right-hand side operator is

defined as

$$F_j(\mathbf{u}) = -\varepsilon u_j \left[\frac{\partial u}{\partial x} \right]_j - \mu \left[\frac{\partial^3 u}{\partial x^3} \right]_j. \quad (41)$$

The spatial derivatives in equation (41) are computed spectrally via equations (38) and (39). The nonlinear term $-\varepsilon u_j (\partial_x u)_j$ introduces quadratic coupling in Fourier space, which may lead to aliasing errors. However, for the resolutions employed in the `sangkuriang` test cases ($N = 512$ or $N = 1024$), these effects remain negligible relative to the specified tolerances [19].

The computational efficiency of the `sangkuriang` solver is significantly enhanced through JIT compilation and parallel processing capabilities provided by Numba [13], a dynamic compiler for Python that translates annotated numerical functions to optimized machine code via the Low Level Virtual Machine (LLVM) compiler infrastructure. The pointwise operations in the nonlinear and dispersive terms of equation (41) are implemented in specialized functions decorated with `@njit(parallel=True, cache=True)`, where the `parallel=True` flag enables automatic parallelization of loops across multiple Central Processing Unit (CPU) cores using Open Multi-Processing (OpenMP)-style threading [13]. Specifically, the elementwise computation of the nonlinear term $-\varepsilon u_j (\partial_x u)_j$ is structured using `prange` (parallel range) rather than Python’s standard `range`, allowing Numba to distribute loop iterations across available processor threads. The `cache=True` option stores compiled machine code to disk, eliminating recompilation overhead in subsequent runs. The number of parallel threads is controlled via `numba.set_num_threads(n)`, where n may be specified by the user or defaults to the total number of available CPU cores detected by the operating system. This parallelization strategy exploits the embarrassingly parallel nature of pointwise arithmetic operations on grid data, though the actual performance gain depends on problem size, memory bandwidth, and hardware architecture—typical speedups range from $5\times$ to $50\times$ compared to interpreted NumPy operations for grid sizes $N \geq 512$ [13]. The JIT compilation overhead is amortized across multiple function calls during time integration, making the optimization particularly effective for the iterative RHS evaluations required by the adaptive time stepper. It should be noted that spectral derivative computations via FFT operations remain implemented in NumPy, as these already employ highly optimized Fastest Fourier Transform in the West (FFTW) or Intel Math Kernel Library (MKL) libraries that are difficult to improve upon with custom JIT compilation.

The semi-discrete system (40) is integrated in time using the DOP853 method [21, 32], an eighth-order explicit Runge–Kutta scheme with embedded fifth and third-order error estimators for adaptive step size control. This method is accessed through `scipy.integrate.solve_ivp` [12] with the `method='DOP853'` option. The DOP853 scheme requires twelve function evaluations per accepted step and provides local error estimates of the form [22]

$$\text{err}_{\text{local}} = \|\mathbf{u}_{n+1}^{(8)} - \mathbf{u}_{n+1}^{(5)}\|, \quad (42)$$

where $\mathbf{u}_{n+1}^{(8)}$ and $\mathbf{u}_{n+1}^{(5)}$ denote the eighth and fifth-order solution approximations at time t_{n+1} , respectively, and $\|\cdot\|$ represents an appropriately weighted norm. The step size adaptation follows the standard embedded method strategy [22]. If the error estimate (42) satisfies

$$\text{err}_{\text{local}} \leq \text{rtol} \cdot \|\mathbf{u}_{n+1}\| + \text{atol}, \quad (43)$$

where `rtol` denotes the relative tolerance and `atol` the absolute tolerance, the step is accepted and the next step size is computed as

$$\Delta t_{n+1} = 0.9 \Delta t_n \left(\frac{\text{rtol} \cdot \|\mathbf{u}_{n+1}\| + \text{atol}}{\text{err}_{\text{local}}} \right)^{1/8}, \quad (44)$$

where the exponent $1/8$ corresponds to the order of the method and the safety factor 0.9 provides robustness against step rejections. If condition (43) is violated, the step is rejected and recomputed with a reduced step size. The `sangkuriang` implementation employs default tolerances of `rtol = 10-10` and `atol = 10-12` for test cases 1–3, and tighter tolerances `rtol = 10-11` and `atol = 10-13` for the more complex three-soliton case 4.

The conservation properties described by equations (30)–(32) serve as critical diagnostics for numerical accuracy [33, 8]. In the oceanographic context, the preservation of these invariants ensures that the numerical solver does not introduce spurious sources or sinks of wave energy or momentum that could distort the simulated soliton dynamics. For the semi-discrete solution $\mathbf{u}(t) = [u_0(t), u_1(t), \dots, u_{N-1}(t)]^T$, these integrals are approximated using the composite trapezoidal rule [34]:

$$M(t) \approx \Delta x \sum_{j=0}^{N-1} u_j(t), \quad (45)$$

$$P(t) \approx \Delta x \sum_{j=0}^{N-1} u_j^2(t), \quad (46)$$

$$E(t) \approx \Delta x \sum_{j=0}^{N-1} \left[\frac{\varepsilon}{2} u_j^3(t) - \frac{3\mu}{2} \left(\frac{\partial u}{\partial x} \right)_j^2(t) \right], \quad (47)$$

where the spatial derivative in equation (47) is computed spectrally via equation (38). The trapezoidal rule achieves second-order accuracy for periodic functions [34], though the spectral accuracy of the solution itself

may allow for higher-order quadrature. The computational implementation uses `numpy.trapz` [11] for numerical integration. The conservation errors are quantified as maximum relative deviations over the simulation time span $[0, T_{\text{final}}]$:

$$\text{err}_M = \max_{t \in [0, T_{\text{final}}]} \frac{|M(t) - M(0)|}{|M(0)|}, \quad (48)$$

$$\text{err}_P = \max_{t \in [0, T_{\text{final}}]} \frac{|P(t) - P(0)|}{|P(0)|}, \quad (49)$$

$$\text{err}_E = \max_{t \in [0, T_{\text{final}}]} \frac{|E(t) - E(0)|}{|E(0)|}. \quad (50)$$

These metrics provide quantitative measures of the numerical method’s ability to preserve the underlying geometric structure of the KdV equation. Conservation errors below 10^{-2} are generally considered acceptable for practical simulations, though the `sangkuriang` implementation typically achieves errors in the range 10^{-6} to 10^{-4} depending on the test case complexity [33].

The complete numerical algorithm proceeds as follows. Given initial condition $u_0(x) = u(x, t = 0)$, we sample at grid points to obtain the initial state vector $\mathbf{u}(0) = [u_0(x_0), u_0(x_1), \dots, u_0(x_{N-1})]^T$. The wavenumber vector $\{k_n\}_{n=0}^{N-1}$ is precomputed according to equation (37) and stored for repeated use in spectral derivative evaluations. The Numba JIT compiler is initialized with the specified number of parallel threads via `set_num_threads(n_cores)`, enabling multi-core parallelization for subsequent RHS evaluations. At each time step, the right-hand side operator (41) is evaluated by: (i) computing the FFT of the current state via equation (35), (ii) multiplying by ik_n and $(ik_n)^3$ to obtain derivative Fourier coefficients, (iii) applying the IFFT via equation (36) to recover physical space derivatives, and (iv) assembling the nonlinear and dispersive terms using JIT-compiled parallel functions. The DOP853 integrator advances the solution from t_n to t_{n+1} according to the adaptive strategy described by equations (43)–(44). At specified output times $\{t_m\}_{m=0}^M$, the solution state is stored and conservation laws (45)–(47) are evaluated for diagnostic purposes. This process continues until the final time T_{final} is reached. The `sangkuriang` numerical implementation leverages established scientific computing libraries widely used in the oceanographic and geoscience communities: NumPy [11] for array operations and FFT routines, SciPy [12] for adaptive ODE integration, Numba [13] for JIT compilation and parallel processing optimization, Matplotlib [35] for visualization, and netCDF4 [23] for scientific data output following CF-1.8 conventions. This combination of spectral methods, high-order adaptive time integration, and parallel computing optimizations may provide both computational efficiency and numerical accuracy appropriate for research-grade simulations of idealized oceanic soliton dynamics.

2.3 Numerical Experiments

The `sangkuriang` solver implementation is validated and demonstrated through four progressively complex test cases that probe different aspects of KdV soliton dynamics relevant to idealized ocean wave propagation. These scenarios are designed to assess: (i) baseline propagation characteristics of isolated solitary waves, as observed when a single internal soliton traverses a continental shelf [46]; (ii) interaction dynamics between equal-amplitude waves, analogous to tidally generated soliton trains with similar amplitudes [49]; (iii) overtaking collision phenomena arising from amplitude-dependent velocities, a common occurrence when faster, larger-amplitude internal waves catch up with smaller predecessors in a wave packet [47, 51]; and (iv) complex multi-body interactions in three-soliton systems, representing the rich dynamics of rank-ordered internal soliton trains frequently observed in satellite imagery of marginal seas [48]. While the `sangkuriang` framework is general and may be applied to arbitrary initial conditions satisfying the periodicity constraint, these canonical test cases provide standardized benchmarks that have been extensively studied in the literature [3, 6, 1] and serve to verify the implementation’s ability to capture the essential physics of nonlinear dispersive wave propagation in shallow water environments.

The first test case examines the propagation of a single soliton in isolation, serving as a baseline reference for subsequent multi-soliton scenarios. This configuration represents the simplest idealization of a solitary internal wave propagating across a flat-bottomed shelf region. The initial condition is specified using the exact single-soliton solution profile (33) in the form

$$u(x, 0) = \frac{A}{\cosh^2 \left[\frac{x-x_0}{w} \right]}, \quad (51)$$

with amplitude $A = 4.0$ m, width parameter $w = 2.0$ m, and initial position $x_0 = -10.0$ m. The computational domain spans $x \in [-30, 30]$ m discretized with $N = 512$ grid points, providing spatial resolution $\Delta x \approx 0.117$ m. The physical parameters are set to $\mu = 0.1$ m³/s and $\varepsilon = 0.2$ m⁻¹, yielding theoretical propagation velocity $v = \varepsilon A/3 \approx 0.267$ m/s according to equation (34). The simulation extends to final time $T_{\text{final}} = 50.0$ s, during which the soliton should traverse approximately 13.3 m while maintaining its shape. This test case validates the `sangkuriang` solver’s ability to preserve soliton structure over extended propagation distances and provides a baseline for assessing conservation law preservation. The expected relative conservation errors for mass, momentum, and energy should remain below 10^{-6} for this smooth, non-interacting solution [33].

The second test case investigates the interaction between two solitons of equal amplitude, which may exhibit phase shift phenomena without energy exchange. This scenario is motivated by observations of tidally generated internal wave packets in which successive solitons emerge with comparable amplitudes from a generation site

such as a sill or shelf break [49, 51]. The initial condition comprises a linear superposition of two sech^2 profiles:

$$u(x, 0) = \frac{A_1}{\cosh^2 \left[\frac{x-x_1}{w_1} \right]} + \frac{A_2}{\cosh^2 \left[\frac{x-x_2}{w_2} \right]}, \quad (52)$$

with identical amplitudes $A_1 = A_2 = 3.0$ m, widths $w_1 = w_2 = 2.0$ m, and symmetrically positioned at $x_1 = -15.0$ m and $x_2 = 15.0$ m. The domain is extended to $x \in [-40, 40]$ m with $N = 512$ points ($\Delta x \approx 0.156$ m), and the simulation time increased to $T_{\text{final}} = 60.0$ s. Since both solitons possess equal amplitudes, they propagate with identical velocities $v = 0.2$ m/s and thus maintain constant separation. However, the initial linear superposition (52) is not an exact solution of the nonlinear KdV equation, necessitating an adjustment phase during which the wave profiles redistribute energy into soliton modes and dispersive radiation [6]. This test case assesses the `sangkuriang` solver’s handling of multi-soliton configurations and the emergence of approximate two-soliton solutions from non-exact initial data. The symmetric configuration also serves as a diagnostic for numerical artifacts, as any asymmetry in the computed solution would indicate spatial discretization errors or inadequate time integration accuracy.

The third test case examines the overtaking collision between solitons of unequal amplitudes, demonstrating the remarkable elastic scattering property that defines soliton behavior. In the ocean, such overtaking events occur routinely when a train of rank-ordered internal solitary waves propagates across a shelf, with the leading (largest) soliton moving fastest according to the amplitude–velocity relation (34), and occasionally overtaking smaller waves that were generated earlier or at a different source [47, 48]. The initial condition takes the form of equation (52) with asymmetric parameters: $A_1 = 6.0$ m, $w_1 = 1.5$ m, $x_1 = -18.0$ m for the leading (taller) soliton, and $A_2 = 2.0$ m, $w_2 = 2.5$ m, $x_2 = -5.0$ m for the trailing (shorter) soliton. According to the velocity relation (34), the taller soliton propagates at $v_1 = 0.4$ m/s while the shorter moves at $v_2 \approx 0.133$ m/s, ensuring that the faster wave overtakes the slower one during the simulation. The domain spans $x \in [-40, 40]$ m with $N = 512$ points, and the final time is extended to $T_{\text{final}} = 70.0$ s to observe the complete collision sequence and subsequent separation. This scenario probes the nonlinear interaction dynamics most severely, as the collision involves significant amplitude modulation and temporary waveform distortion [3]. The remarkable theoretical prediction—that both solitons emerge from the collision with their original amplitudes and velocities intact, differing only by phase shifts—provides a stringent test of the numerical method’s ability to capture the integrable structure of the KdV equation [5]. Conservation errors may increase during the collision phase due to enhanced nonlinearity, but should remain below 10^{-4} for the employed tolerances.

The fourth test case extends the complexity to a three-soliton system, creating a choreography of multiple interactions that tests the `sangkuriang` solver’s robustness under more challenging conditions. This configuration serves as an idealized representation of the rank-ordered internal soliton packets widely documented in the South China Sea, the Strait of Gibraltar, and other energetic oceanic environments, where three or more solitary waves of decreasing amplitude propagate as a coherent group [46, 49]. The initial condition generalizes equation (52) to three components:

$$u(x, 0) = \sum_{j=1}^3 \frac{A_j}{\cosh^2 \left[\frac{x-x_j}{w_j} \right]}, \quad (53)$$

with amplitudes $A_1 = 7.0$ m, $A_2 = 4.0$ m, $A_3 = 2.5$ m, widths $w_1 = 1.2$ m, $w_2 = 1.8$ m, $w_3 = 2.2$ m, and initial positions $x_1 = -25.0$ m, $x_2 = -10.0$ m, $x_3 = 5.0$ m, respectively. The corresponding velocities are $v_1 \approx 0.467$ m/s, $v_2 \approx 0.267$ m/s, and $v_3 \approx 0.167$ m/s, ordered such that each faster soliton will sequentially overtake the slower ones ahead. To accommodate the increased spatial extent of the three-wave system and provide adequate resolution for the narrowest soliton, the domain is enlarged to $x \in [-50, 50]$ m with enhanced resolution $N = 1024$ ($\Delta x \approx 0.098$ m). The simulation extends to $T_{\text{final}} = 80.0$ s with tightened tolerances $\text{rtol} = 10^{-11}$ and $\text{atol} = 10^{-13}$ to maintain accuracy through multiple collision events. This test case may exhibit complex interaction patterns including transient amplitude amplifications during collisions, the generation of small-amplitude dispersive radiation, and intricate phase shift accumulations [6, 1]. The successful navigation of these multiple interactions while preserving conservation laws and soliton identities demonstrates the `sangkuriang` solver’s capability for research-grade simulations of multi-soliton dynamics relevant to oceanic internal wave studies.

The physical parameters $\mu = 0.1$ m³/s and $\varepsilon = 0.2$ m⁻¹ are held constant across all test cases to facilitate direct comparison of dynamical behaviors. These values are representative of the weakly nonlinear, weakly dispersive regime characteristic of long gravity waves in shallow coastal waters [26], and ensure that the balance between nonlinearity and dispersion falls within the regime where soliton solutions are well-defined. The specific choices of soliton amplitudes and positions in each test case are informed by established benchmarks in the soliton literature [3, 20] and are designed to produce qualitatively distinct interaction scenarios within computationally tractable simulation times. While these four cases provide comprehensive validation of the `sangkuriang` solver’s core functionality, the implementation supports arbitrary initial conditions through the `SechProfile`, `TanhProfile`, `GaussianProfile`, and `MultiSoliton` classes, enabling users to investigate alternative scenarios such as soliton generation from non- sech^2 initial data, wave packet decomposition, or soliton interactions with continuous wave backgrounds—all of which are relevant to understanding observed oceanic internal wave phenomena [50, 51].

The output from each `sangkuriang` simulation includes the complete spatiotemporal field $u(x, t)$, conservation law time series $M(t)$, $P(t)$, $E(t)$ as defined in equations (45)–(47), relative conservation errors (48)–(50), and

diagnostic information regarding computational cost (number of function evaluations, wall clock time). Data are stored in netCDF4 format [23] following CF-1.8 metadata conventions, facilitating interoperability with standard oceanographic data analysis tools and ensuring compatibility with widely used geoscience software packages. Animated visualizations are generated showing the evolving wave profile in three-dimensional space-time representations, with conservation law diagnostics overlaid to provide immediate visual feedback on solution quality. These outputs enable both qualitative assessment of soliton dynamics and quantitative verification of the numerical implementation’s fidelity to the underlying physics encoded in the KdV equation (29).

2.4 Data Analysis

The diagnostic analysis of simulation outputs is performed independently of the `sangkuriang` solver library through a dedicated suite of post-processing routines implemented in Python. These routines employ NumPy [11] for array operations and FFT, SciPy [12] for signal processing and distance computations, and Matplotlib [35] for visualization. Simulation data archived in netCDF4 format [23] following CF-1.8 conventions are subjected to four complementary analyses: verification of conservation law preservation, soliton trajectory tracking with velocity validation, spectral information-theoretic characterization, and phase space recurrence quantification. Each analysis extracts quantitative metrics that collectively assess both numerical accuracy and physical fidelity of the computed solutions. Together, these diagnostics provide a comprehensive assessment framework applicable not only to the idealized KdV system studied here but also to more complex ocean wave models where analytical benchmarks may be unavailable [50, 51].

The conservation analysis quantifies the temporal stability of the three KdV invariants defined in equations (45)–(47). Let $Q(t)$ denote any of the conserved quantities $M(t)$, $P(t)$, or $E(t)$ evaluated at discrete output times $\{t_n\}_{n=0}^{N_t-1}$, where N_t is the total number of stored time snapshots. The instantaneous relative deviation from the initial state is defined as

$$\delta_Q(t_n) = \frac{Q(t_n) - Q(t_0)}{|Q(t_0)|}, \quad (54)$$

which measures the fractional departure of Q from its initial value $Q(t_0) = Q_0$. Three statistical measures characterize the behavior of δ_Q over the simulation interval. The maximum relative error,

$$\text{err}_Q = \max_{0 \leq n < N_t} |\delta_Q(t_n)|, \quad (55)$$

captures the worst-case deviation and is stored directly in the netCDF output files. The RMS error,

$$\sigma_Q = \left[\frac{1}{N_t} \sum_{n=0}^{N_t-1} \delta_Q^2(t_n) \right]^{1/2}, \quad (56)$$

provides a time-averaged measure of conservation fidelity that is less sensitive to isolated outliers. To distinguish systematic drift from bounded oscillations—a distinction important for assessing whether numerical errors would accumulate to unphysical levels over the long propagation distances typical of oceanic solitary waves—the linear drift rate γ_Q is extracted via ordinary least-squares regression. Defining the design matrix $\mathbf{A} \in \mathbb{R}^{N_t \times 2}$ with elements $A_{n1} = t_n$ and $A_{n2} = 1$, and the observation vector $\mathbf{b} = [\delta_Q(t_0), \delta_Q(t_1), \dots, \delta_Q(t_{N_t-1})]^T$, the drift rate is obtained as the first component of the least-squares solution

$$[\gamma_Q, \beta_Q]^T = (\mathbf{A}^T \mathbf{A})^{-1} \mathbf{A}^T \mathbf{b}, \quad (57)$$

where β_Q is an intercept term. A nonzero γ_Q [s⁻¹] indicates secular accumulation of numerical error, whereas $\gamma_Q \approx 0$ with finite σ_Q suggests oscillatory but bounded deviations consistent with symplectic or near-symplectic integration.

Soliton trajectory extraction proceeds through systematic identification and tracking of local amplitude maxima in the spatiotemporal field $u(x_j, t_n)$. This procedure is analogous to the peak-tracking methods employed in observational oceanography to identify and follow individual internal solitary waves in mooring time series or satellite image sequences [47, 49]. At each output time t_n , the discrete spatial profile $\{u_j^{(n)}\}_{j=0}^{N-1} \equiv \{u(x_j, t_n)\}_{j=0}^{N-1}$ is analyzed using the `scipy.signal.find_peaks` routine [12], which identifies indices j^* satisfying $u_{j^*}^{(n)} > u_{j^*-1}^{(n)}$, $u_{j^*}^{(n)} > u_{j^*+1}^{(n)}$, subject to additional constraints. Two filtering parameters govern peak selection: a height threshold u_{th} requiring $u_{j^*}^{(n)} > u_{\text{th}}$, and a minimum separation distance d_{min} (in grid points) enforcing $|j_1^* - j_2^*| > d_{\text{min}}$ between distinct peaks. For the test cases examined, $u_{\text{th}} = 0.5$ m for multi-soliton configurations and $u_{\text{th}} = 1.0$ m for single-soliton runs, with $d_{\text{min}} = 10$ grid points throughout. Each detected peak yields a triplet $(t_n, x_{j^*}, u_{j^*}^{(n)})$ recording the time, spatial position, and amplitude.

For configurations containing K solitons, individual trajectories must be disambiguated from the aggregate peak data. This is accomplished through amplitude-based sorting at each time instant: letting $\{(x_k^{(n)}, A_k^{(n)})\}_{k=1}^{K_n}$ denote the K_n peaks detected at time t_n with positions $x_k^{(n)}$ and amplitudes $A_k^{(n)}$, these are reordered such that $A_1^{(n)} \geq A_2^{(n)} \geq \dots \geq A_{K_n}^{(n)}$. The k -th soliton track is then defined as the sequence $\{(t_n, x_k^{(n)})\}$ across all times where at least k peaks were detected. This ranking scheme exploits the amplitude-velocity ordering inherent to KdV solitons: since taller solitons propagate faster according to equation (34), amplitude rank provides a consistent identifier even through collision events where spatial ordering temporarily inverts. The same amplitude-rank

ordering is a well-known feature of oceanic internal solitary wave packets, where the leading wave is typically the largest [46, 48].

The propagation velocity of each tracked soliton is determined by linear regression of position against time. For the k -th soliton trajectory restricted to a temporal window $[t_a, t_b]$ containing N_k data points, the measured velocity v_k^{meas} minimizes the sum of squared residuals:

$$v_k^{\text{meas}} = \arg \min_v \sum_{n: t_n \in [t_a, t_b]} \left[x_k^{(n)} - vt_n - x_k^{(0)} \right]^2. \quad (58)$$

The explicit solution via `numpy.polyfit` [11] yields v_k^{meas} as the slope of the fitted line $x_k(t) = v_k^{\text{meas}}t + x_k^{(0)}$. Goodness-of-fit is quantified by the coefficient of determination

$$R_k^2 = 1 - \frac{\sum_n (x_k^{(n)} - v_k^{\text{meas}}t_n - x_k^{(0)})^2}{\sum_n (x_k^{(n)} - \bar{x}_k)^2}, \quad (59)$$

where $\bar{x}_k = N_k^{-1} \sum_n x_k^{(n)}$ is the mean position. Values $R_k^2 \rightarrow 1$ indicate linear trajectories consistent with constant-velocity propagation. The mean soliton amplitude over the fitting interval,

$$\bar{A}_k = \frac{1}{N_k} \sum_{n: t_n \in [t_a, t_b]} A_k^{(n)}, \quad (60)$$

together with its standard deviation σ_{A_k} , enables comparison against the theoretical velocity relation (34). The theoretical prediction $v_k^{\text{theo}} = \varepsilon \bar{A}_k / 3$ should match v_k^{meas} for well-resolved soliton solutions, providing validation of both numerical accuracy and the soliton character of computed waveforms.

Spectral analysis employs the DFT (35) to characterize the wavenumber content of each spatial snapshot. For the field $\{u_j^{(n)}\}_{j=0}^{N-1}$ at time t_n , the power spectral density is computed as

$$P_m^{(n)} = \frac{1}{N} |\hat{u}_m^{(n)}|^2, \quad m = 0, 1, \dots, N-1, \quad (61)$$

where $\hat{u}_m^{(n)}$ denotes the m -th Fourier coefficient obtained via `numpy.fft.fft` [11]. The corresponding wavenumbers k_m follow from equation (37) and are generated using `numpy.fft.fftfreq`. Normalization of the power spectrum yields a discrete probability distribution over wavenumber space:

$$p_m^{(n)} = \frac{P_m^{(n)}}{\sum_{\ell=0}^{N-1} P_\ell^{(n)}}, \quad \sum_{m=0}^{N-1} p_m^{(n)} = 1, \quad (62)$$

representing the fractional energy content at wavenumber k_m . This spectral probability distribution forms the basis for three information-theoretic measures that characterize distinct aspects of the wave field structure.

The spectral entropy [36] quantifies the breadth of spectral energy distribution through the normalized Shannon entropy of $\{p_m^{(n)}\}$:

$$S_k^{(n)} = -\frac{1}{\ln N} \sum_{m=0}^{N-1} p_m^{(n)} \ln p_m^{(n)}, \quad (63)$$

where terms with $p_m^{(n)} < 10^{-15}$ are excluded from the summation to avoid numerical singularities. The normalization by $\ln N$ ensures $S_k^{(n)} \in [0, 1]$, with $S_k^{(n)} = 0$ corresponding to a monochromatic signal (all energy concentrated at a single wavenumber) and $S_k^{(n)} = 1$ to uniform spectral distribution (white noise). Soliton profiles, characterized by smooth sech^2 envelopes with exponentially decaying Fourier spectra, exhibit intermediate entropy values that remain approximately constant during propagation. Changes in spectral entropy during soliton interactions provide a measure of how the wave field's spectral complexity evolves—information that is relevant to understanding energy cascades in oceanic internal wave fields [51].

The López-Ruiz-Mancini-Calbet (LMC) statistical complexity [37] captures the interplay between disorder and departure from equilibrium through the product

$$C_{\text{LMC}}^{(n)} = H^{(n)} \times D^{(n)}, \quad (64)$$

where $H^{(n)} = S_k^{(n)}$ is the normalized spectral entropy defined in equation (63), and the disequilibrium

$$D^{(n)} = \sum_{m=0}^{N-1} \left(p_m^{(n)} - \frac{1}{N} \right)^2 \quad (65)$$

measures the squared Euclidean distance between the observed distribution $\{p_m^{(n)}\}$ and the uniform distribution $\{1/N\}$. This construction ensures $C_{\text{LMC}}^{(n)} = 0$ for both perfectly ordered states ($H^{(n)} = 0$, all energy at one mode) and maximally disordered states ($D^{(n)} = 0$, uniform distribution), attaining nonzero values only for intermediate configurations exhibiting nontrivial structure [37]. The LMC complexity thus distinguishes structured nonequilibrium states from both trivial order and featureless randomness, offering a single scalar diagnostic for the degree of organized wave structure in the computed solutions.

The Fisher information [38, 39, 40] provides a complementary characterization of spatial localization by measuring the “sharpness” of the amplitude distribution. Defining the normalized spatial probability density

$$\rho_j^{(n)} = \frac{|u_j^{(n)}| + \epsilon_{\text{reg}}}{\sum_{\ell=0}^{N-1} (|u_\ell^{(n)}| + \epsilon_{\text{reg}}) \Delta x}, \quad (66)$$

where $\epsilon_{\text{reg}} = 10^{-15}$ is a regularization parameter preventing division by zero, the discrete Fisher information is computed as

$$F^{(n)} = \sum_{j=0}^{N-1} \frac{1}{\rho_j^{(n)}} \left(\frac{\partial \rho}{\partial x} \Big|_j^{(n)} \right)^2 \Delta x. \quad (67)$$

The spatial derivative $(\partial_x \rho)_j^{(n)}$ is evaluated using second-order central differences via `numpy.gradient` [11]:

$$\frac{\partial \rho}{\partial x} \Big|_j^{(n)} \approx \frac{\rho_{j+1}^{(n)} - \rho_{j-1}^{(n)}}{2\Delta x}, \quad (68)$$

with one-sided differences at domain boundaries. Higher Fisher information indicates sharper spatial gradients and hence more localized wave structures; for soliton solutions, $F^{(n)}$ scales inversely with the characteristic width parameter w appearing in equation (33). During soliton collisions, transient increases in $F^{(n)}$ reflect the temporary steepening of gradients as wave profiles overlap, providing a quantitative signature of the interaction events that parallels the steepening observed in field measurements of colliding internal solitary waves [47].

Phase space analysis employs recurrence quantification analysis (RQA) [41, 42] to characterize the dynamical structure of simulation trajectories. For integrable Hamiltonian systems possessing multiple conservation laws, trajectories are confined to low-dimensional invariant manifolds in the full phase space; deviations from this structure would indicate either numerical error or departure from integrability. The analysis proceeds by embedding the temporal evolution in a three-dimensional conservation space with coordinates

$$\mathbf{y}^{(n)} = \left(\frac{M(t_n)}{M_0}, \frac{P(t_n)}{P_0}, \frac{E(t_n)}{E_0} \right)^T \in \mathbb{R}^3, \quad (69)$$

where normalization by initial values M_0, P_0, E_0 renders the components dimensionless and of comparable magnitude. For a perfectly conservative numerical scheme, $\mathbf{y}^{(n)} = (1, 1, 1)^T$ for all n ; deviations from this ideal point trace out a trajectory reflecting cumulative numerical errors.

The pairwise Euclidean distance matrix $\mathbf{D} \in \mathbb{R}^{N_t \times N_t}$ with elements

$$D_{ij} = \|\mathbf{y}^{(i)} - \mathbf{y}^{(j)}\| = \left[\sum_{\alpha=1}^3 (y_\alpha^{(i)} - y_\alpha^{(j)})^2 \right]^{1/2} \quad (70)$$

is computed efficiently using `scipy.spatial.distance.pdist` and `squareform` [12]. A recurrence threshold ϵ is determined adaptively as the q -th percentile of the nonzero elements of \mathbf{D} , with $q = 10$ –15 providing robust results across test cases. The binary recurrence matrix [41] is then constructed as

$$R_{ij} = \Theta(\epsilon - D_{ij}) = \begin{cases} 1, & D_{ij} < \epsilon, \\ 0, & D_{ij} \geq \epsilon, \end{cases} \quad (71)$$

where $\Theta(\cdot)$ denotes the Heaviside step function. By construction, $R_{ii} = 1$ for all i (self-recurrence), and $R_{ij} = R_{ji}$ (symmetry).

Two scalar metrics extracted from the recurrence matrix characterize the dynamical behavior. The recurrence rate

$$\text{RR} = \frac{1}{N_t(N_t - 1)} \sum_{\substack{i,j=0 \\ i \neq j}}^{N_t-1} R_{ij} \quad (72)$$

quantifies the density of recurrent pairs, excluding the trivial diagonal $i = j$. Higher RR indicates that the trajectory repeatedly visits similar regions of conservation space, consistent with bounded oscillatory errors rather than secular drift. The determinism

$$\text{DET} = \frac{\sum_{\ell \geq \ell_{\min}} \ell \cdot P(\ell)}{\sum_{i \neq j} R_{ij}} \quad (73)$$

measures the fraction of recurrence points forming diagonal line structures of length at least ℓ_{\min} (typically $\ell_{\min} = 2$). Here $P(\ell)$ denotes the number of diagonal lines of exactly length ℓ in the recurrence matrix, where a diagonal line at offset $k > 0$ consists of consecutive entries $R_{i,i+k} = R_{i+1,i+1+k} = \dots = 1$. Diagonal structures arise when segments of the trajectory evolve in parallel, a hallmark of deterministic dynamics on regular (non-chaotic) attractors [42]. For integrable systems such as the KdV equation, $\text{DET} \rightarrow 1$ reflects confinement to invariant tori, whereas chaotic systems exhibit $\text{DET} \ll 1$ due to sensitive dependence on initial conditions disrupting parallel trajectory segments. In the context of ocean wave dynamics, high determinism values provide confidence that the numerical solver faithfully preserves the regular dynamical structure expected of the idealized KdV system,

which is a prerequisite for reliable long-time simulations of solitary wave propagation and interaction [6].

Complementary phase space characterization is obtained through analysis of Fourier mode amplitudes. The leading K complex Fourier coefficients $\{\hat{u}_m^{(n)}\}_{m=0}^{K-1}$ (typically $K = 3-5$) extracted from each temporal snapshot define a trajectory in a $2K$ -dimensional space (accounting for real and imaginary parts). Projection onto the real components of the first two modes, $(\text{Re}[\hat{u}_0^{(n)}], \text{Re}[\hat{u}_1^{(n)}])$, yields a two-dimensional phase portrait that visualizes the modal dynamics. For the KdV equation, the zeroth mode $\hat{u}_0^{(n)} = N^{-1} \sum_j u_j^{(n)}$ is proportional to the spatial mean (and hence to the mass M), while higher modes capture spatial structure. Bounded, closed orbits in this projection confirm the quasi-periodic character expected of integrable dynamics, whereas space-filling or divergent trajectories would signal chaotic or unstable behavior.

3 Results

The `sangkuriang` solver was validated through four test cases of increasing complexity, executed on a laptop-class workstation (Lenovo ThinkPad P52s with Intel Core i7-8550U processor at 4.0 GHz, 8 logical cores) running Fedora Linux 39 (kernel 6.11.9-100.fc39.x86_64). This hardware configuration represents a modest computational platform typical of those available to individual researchers in oceanography and geoscience departments, permitting assessment of the solver’s practical utility for idealized ocean wave studies without access to high-performance computing resources.

Table 1 summarizes the computational cost for each test case. The single-soliton simulation (Case 1) required 208,202 adaptive time steps to integrate over the 50 s interval, completing in approximately 152 s of wall-clock time. The adaptive time stepper selected finer temporal resolution for this case due to the smaller spatial domain ($L = 60$ m) and correspondingly higher wavenumber content relative to Cases 2 and 3. The two equal-amplitude soliton simulation (Case 2) completed in 75.7 s using 98,612 steps, while the overtaking collision (Case 3) required 115,658 steps and 87.6 s. The three-soliton configuration (Case 4), employing doubled spatial resolution ($N = 1024$) and tightened tolerances ($\text{rtol} = 10^{-11}$, $\text{atol} = 10^{-13}$), demanded 551,858 steps and 534 s of computation time. These timings suggest that the Numba-accelerated implementation achieves reasonable throughput for exploratory research into idealized ocean wave dynamics, though the scaling with grid resolution and tolerance warrants consideration for production simulations involving extended ocean domains.

Table 1: Computational performance metrics for the four test cases. All simulations employed 8 parallel threads via Numba JIT compilation.

Case	N	Δx [m]	T_{final} [s]	Steps	CPU Time [s]
1 (Single soliton)	512	0.117	50	208,202	152.0
2 (Two equal)	512	0.157	60	98,612	75.7
3 (Collision)	512	0.157	70	115,658	87.6
4 (Three solitons)	1024	0.098	80	551,858	534.4

The throughput, measured in time steps per second, remained relatively consistent across Cases 1–3 at approximately 1300–1370 steps/s, decreasing to roughly 1030 steps/s for Case 4. This reduction likely reflects the increased memory bandwidth demands associated with the larger grid and the superlinear scaling of FFT operations, which nominally follow $\mathcal{O}(N \log N)$ complexity [30]. Nevertheless, all simulations completed within times amenable to interactive research workflows, enabling rapid parameter exploration in idealized ocean soliton studies.

The preservation of the three KdV invariants—mass M , momentum P , and energy E as defined in equations (45)–(47)—provides a stringent test of numerical accuracy. For ocean wave applications, the faithful conservation of these quantities ensures that the solver does not introduce spurious wave energy sources or sinks that could contaminate the simulated dynamics [33]. Figure 2 displays the temporal evolution of relative conservation errors for all test cases.

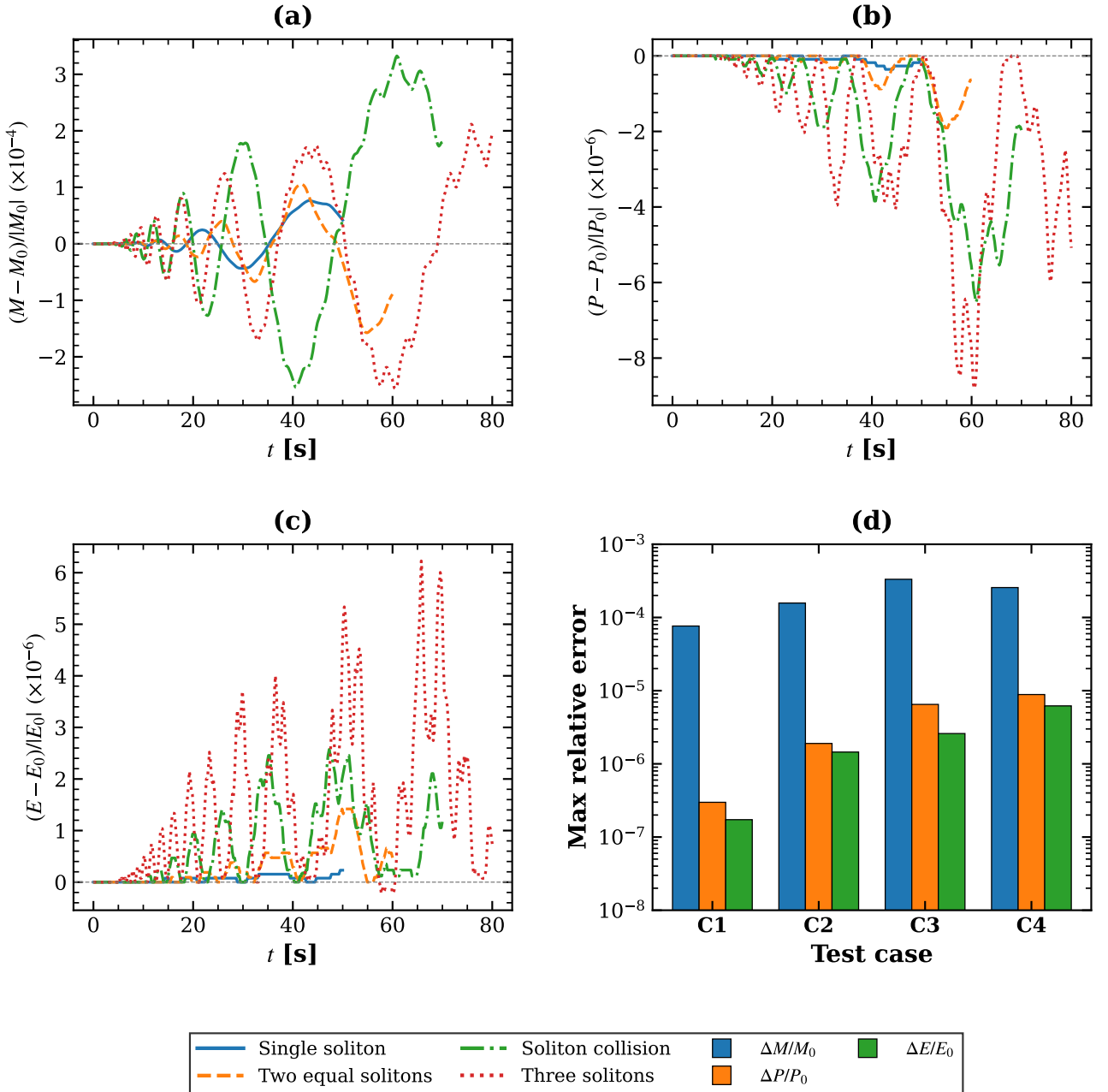


Figure 2: Conservation law diagnostics. (a) Relative mass deviation $(M - M_0)/|M_0|$; (b) relative momentum deviation $(P - P_0)/|P_0|$; (c) relative energy deviation $(E - E_0)/|E_0|$; (d) maximum relative errors across all cases on logarithmic scale. Solid blue: single soliton (C1); dashed orange: two equal solitons (C2); dash-dotted green: soliton collision (C3); dotted red: three solitons (C4).

The single-soliton case exhibited the smallest conservation errors, with maximum relative deviations of 7.64×10^{-5} for mass, 2.98×10^{-7} for momentum, and 1.73×10^{-7} for energy. These values are consistent with the specified integration tolerances and confirm that the pseudo-spectral spatial discretization introduces negligible additional error for smooth, non-interacting solutions representative of an isolated oceanic solitary wave. The root-mean-square (RMS) errors were approximately half the maximum values (3.55×10^{-5} , 1.30×10^{-7} , and 8.28×10^{-8} , respectively), indicating that the deviations represent bounded oscillations rather than secular drift. Linear regression of the conservation time series yielded drift rates on the order of 10^{-9} s^{-1} for momentum and energy, suggesting that the dominant error contribution arises from the non-symplectic character of the DOP853 integrator rather than from systematic bias [22].

Multi-soliton configurations exhibited moderately larger conservation errors, as anticipated from the increased solution complexity during interaction events. The two equal-amplitude soliton case (Case 2) showed maximum errors of 1.57×10^{-4} (mass), 1.90×10^{-6} (momentum), and 1.45×10^{-6} (energy). The overtaking collision (Case 3) produced the largest mass error at 3.33×10^{-4} , with momentum and energy errors of 6.49×10^{-6} and 2.60×10^{-6} , respectively. Figure 2a–c reveals that the conservation deviations exhibit transient excursions correlated with

collision events, particularly evident in the three-soliton case where multiple interactions occur. Such transient increases in conservation error during wave-wave interaction are expected physically, as the nonlinear coupling intensifies when soliton profiles overlap [6]. Despite the increased complexity of Case 4, the maximum errors (2.56×10^{-4} , 8.86×10^{-6} , 6.20×10^{-6}) remained comparable to or smaller than those of Case 3, likely reflecting the benefits of enhanced spatial resolution and tighter tolerances employed for this configuration.

The bar chart in Figure 2d presents a comparative summary of maximum relative errors across all cases. A consistent hierarchy emerges: mass conservation errors exceed momentum errors by approximately two orders of magnitude, which in turn exceed energy errors. This ordering may reflect the different sensitivities of each integral to high-wavenumber components of the solution, with the energy functional (32) involving spatial derivatives that weight the well-resolved low-wavenumber content more heavily. Across all test cases, the conservation errors remain well below the 10^{-2} threshold commonly adopted as acceptable for practical simulations of Hamiltonian systems [33], suggesting that the `sangkuriang` implementation maintains adequate fidelity to the underlying physics governing idealized ocean soliton propagation.

Figure 3 presents three-dimensional visualizations of the wave field $u(x,t)$ for each test case, rendered with consistent axis limits ($x \in [-50, 50]$ m, $t \in [0, 80]$ s, $u \in [0, 9]$ m) to facilitate direct comparison of the idealized oceanic soliton dynamics.

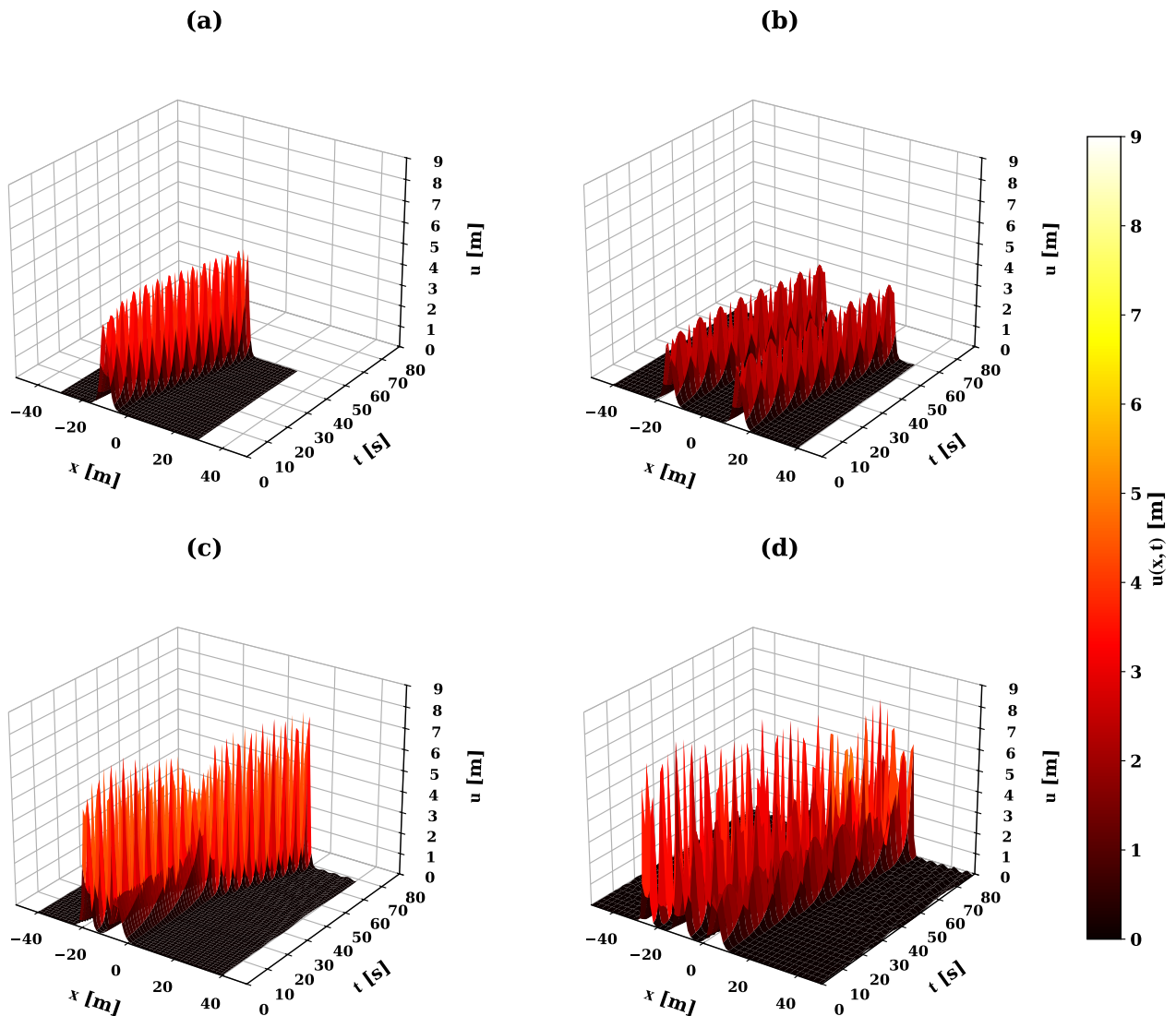


Figure 3: Three-dimensional spatiotemporal evolution of the wave amplitude $u(x,t)$ for the four test cases. (a) Single soliton propagating rightward; (b) two equal-amplitude solitons; (c) overtaking collision between fast (tall) and slow (short) solitons; (d) three-soliton interaction. Color scale indicates amplitude in meters. View angles: elevation 25° , azimuth -55° .

Panel (a) illustrates the single-soliton case, where the initial sech^2 profile propagates from left to right while maintaining its characteristic shape—the hallmark of a solitary wave in a dispersive medium. The wave amplitude increases slightly from the initial value of approximately 4.0 m to a final peak of 5.2 m, with a global maximum of

5.21 m observed during the simulation. This amplitude evolution reflects the adjustment of the initial condition—which approximates but does not precisely match the exact soliton solution (33)—toward a true soliton state through radiation of small-amplitude dispersive waves [6]. Such adjustment dynamics are analogous to the fission process observed when a tidal bore or internal tide evolves into a rank-ordered train of solitary waves on a continental shelf [46, 49]. The peak position advanced by 17.8 m over the 50 s integration interval, corresponding to an average velocity of 0.357 m/s.

The two equal-amplitude soliton configuration, shown in panel (b), exhibits parallel propagation of two $A = 3.0$ m solitons initially separated by 30 m. Since the KdV soliton velocity is proportional to amplitude according to equation (34), these waves maintain constant separation throughout the simulation, akin to the approximately equal-amplitude internal waves sometimes observed in the trailing portion of oceanic soliton packets [48]. The surface plot reveals two distinct ridges traversing the space-time domain without intersection, confirming the expected kinematic behavior. Minor amplitude variations (final peak 3.66 m versus initial 3.0 m) again indicate adjustment toward exact soliton profiles.

Panel (c) displays the overtaking collision scenario, which constitutes the most stringent test of the solver’s ability to capture nonlinear interaction dynamics. The taller soliton ($A_1 = 6.0$ m), propagating faster than the shorter wave ($A_2 = 2.0$ m), overtakes and passes through it near $t \approx 35$ s and $x \approx 0$ m. The characteristic “X”-shaped intersection pattern in the space-time surface demonstrates the elastic scattering property of KdV solitons: both waves emerge from the collision with their identities intact, differing only by phase shifts [3]. This elastic interaction is the idealized analog of the overtaking collisions documented in field observations of internal solitary waves, where larger waves catch and pass smaller ones with remarkably little energy exchange [47, 51]. The global maximum amplitude of 7.55 m, exceeding the linear superposition of the two initial amplitudes, reflects the transient nonlinear amplification during the collision phase.

The three-soliton interaction in panel (d) presents the most complex dynamics, with multiple collision events occurring as the fastest soliton ($A_1 = 7.0$ m) successively overtakes the intermediate ($A_2 = 4.0$ m) and slowest ($A_3 = 2.5$ m) waves. The space-time surface exhibits a sequence of intersection patterns, with a global maximum of 8.26 m observed during the highest-amplitude collision. Despite this complexity, the three distinct soliton tracks remain identifiable throughout the simulation, consistent with the complete integrability of the KdV equation [4]. This rank-ordered configuration, with the largest and fastest wave leading, mirrors the structure of oceanic internal soliton packets routinely observed in satellite synthetic aperture radar imagery [46, 49].

Quantitative validation of the soliton dynamics requires comparison of measured propagation velocities against theoretical predictions. Figure 4 presents trajectory data extracted from the spatiotemporal fields using peak detection and tracking algorithms.

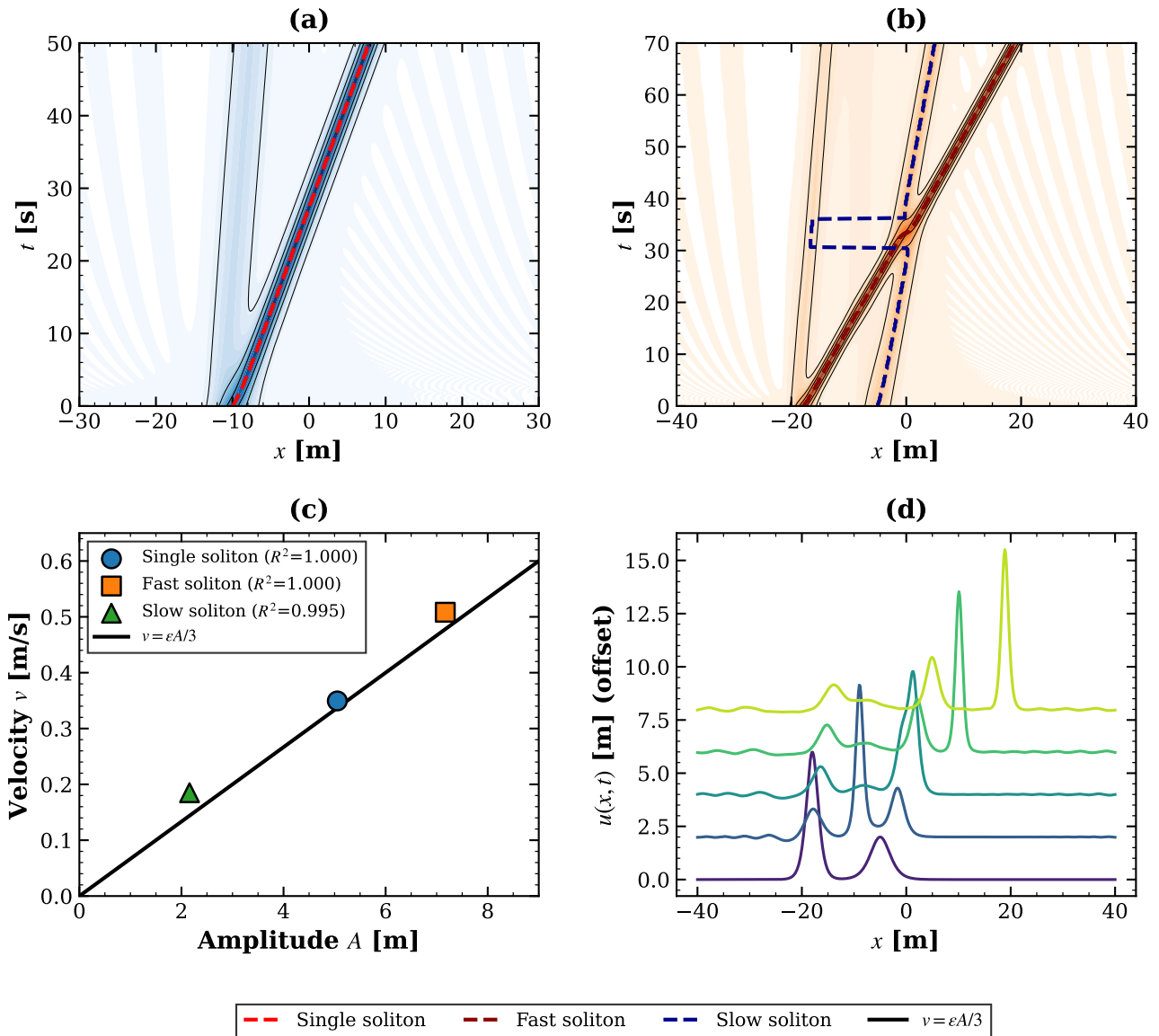


Figure 4: Soliton trajectory analysis. (a) Space-time contour plot for single soliton with tracked trajectory (dashed line); (b) collision case showing fast (dark red) and slow (blue) soliton tracks with collision region indicated; (c) measured velocity versus amplitude with theoretical relation $v = \epsilon A/3$ (solid line); (d) wave profiles at selected times during collision, vertically offset for clarity.

Panel (a) displays the single-soliton trajectory as a space-time contour plot with the tracked peak position overlaid. The trajectory exhibits excellent linearity, with a coefficient of determination $R^2 = 0.9998$ for the linear fit. The measured amplitude of 5.05 ± 0.29 m (mean \pm standard deviation over the simulation) yields a theoretical velocity of $v_{\text{theo}} = \epsilon A/3 = 0.337$ m/s according to equation (34). The measured velocity of 0.349 m/s exceeds this prediction by approximately 3.6%, a discrepancy that may be attributed to the amplitude evolution during the initial adjustment phase.

The collision case trajectories, shown in panel (b), reveal the characteristic behavior of an overtaking interaction. The fast soliton (amplitude 7.17 ± 0.39 m) propagates at a measured velocity of 0.508 m/s with $R^2 = 0.9995$, while the slow soliton (amplitude 2.16 ± 0.10 m) travels at 0.185 m/s with $R^2 = 0.9950$. The slightly reduced R^2 value for the slow soliton reflects the greater relative perturbation experienced during the collision. The dashed box in panel (b) highlights the collision region where the trajectories temporarily merge before separating.

Panel (c) synthesizes the velocity–amplitude relationship across all tracked solitons. The data points cluster along the theoretical line $v = \epsilon A/3$, providing quantitative confirmation that the computed solutions satisfy the fundamental KdV dispersion relation. The agreement is particularly notable given that the initial conditions employ approximate sech^2 profiles rather than exact soliton solutions, demonstrating the robustness of the soliton state as an attractor in the KdV phase space [1]. This amplitude–velocity scaling is the same relationship that governs the rank ordering and separation of internal solitary waves observed in the ocean [46, 48].

Panel (d) presents a sequence of wave profiles during the collision event, vertically offset for visualization.

The temporal progression illustrates the collision mechanism: the faster soliton approaches from behind, the two waves temporarily merge into a single enhanced peak, and subsequently separate with their original amplitudes restored. This elastic scattering behavior, wherein solitons interact nonlinearly yet emerge unchanged, constitutes the defining characteristic that distinguishes solitons from ordinary dispersive wave packets [3].

Beyond trajectory analysis, the spectral structure and information content of the wave field provide complementary diagnostics of solution quality. Figure 5 presents four measures characterizing different aspects of the spatial Fourier decomposition and its evolution.

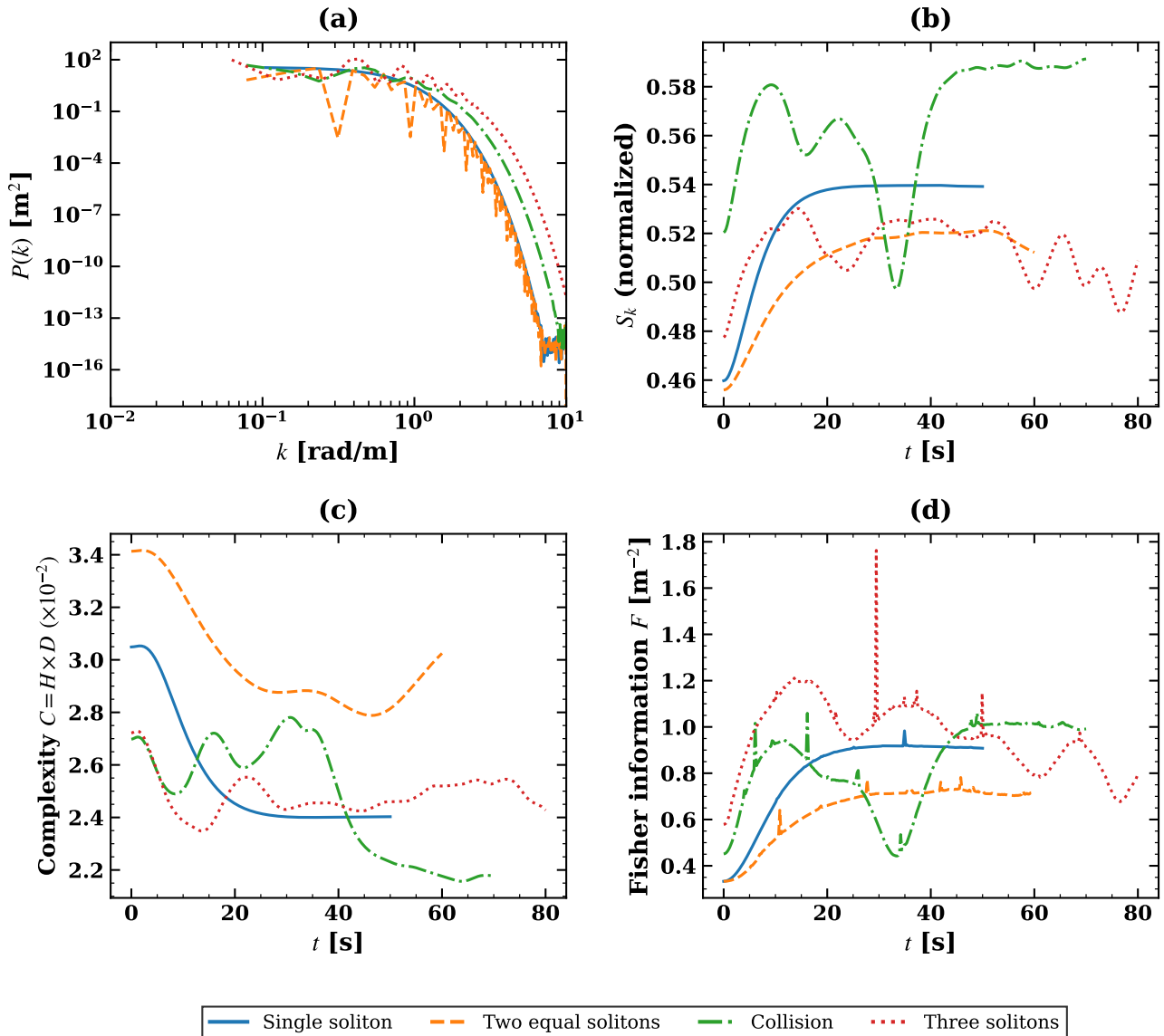


Figure 5: Spectral and information-theoretic analysis. (a) Power spectral density $P(k)$ at initial time for all cases; (b) normalized spectral entropy $S_k(t)$; (c) LMC statistical complexity $C(t) = H \times D$; (d) Fisher information $F(t)$. Line styles as in Figure 2.

Panel (a) displays the initial power spectral density $P(k)$ on logarithmic axes. All cases exhibit similar spectral structure: a plateau at low wavenumbers ($k < 0.1$ rad/m) transitioning to exponential decay at higher wavenumbers, consistent with the smooth sech^2 spatial profiles characteristic of KdV solitons [18]. The three-soliton case (dotted red) shows the highest total power, reflecting the larger combined amplitude, while the two equal-amplitude case (dashed orange) exhibits oscillatory modulation arising from the spatial interference pattern of the two separated solitons. The spectral decay extends over approximately 15 orders of magnitude before reaching the numerical noise floor near 10^{-16} , confirming that aliasing errors remain negligible for the employed spatial resolutions.

The normalized spectral entropy S_k , plotted in panel (b), quantifies the breadth of the spectral energy distribution according to equation (63). Values near unity indicate uniform spectral content (approaching white noise), while values near zero correspond to energy concentration at a single wavenumber (monochromatic). The

soliton solutions exhibit intermediate values in the range 0.46–0.59, reflecting their localized but smooth spatial structure. The single-soliton case shows relatively stable entropy (0.528 ± 0.021), while the collision case displays larger fluctuations (0.567 ± 0.024) with transient increases during the interaction event near $t = 35$ s. These variations suggest temporary spectral broadening as the wave profiles distort during collision, followed by return to the pre-collision distribution as the solitons separate—a spectral signature of the elastic scattering process.

The LMC statistical complexity $C = H \times D$, shown in panel (c), provides a measure that distinguishes structured states from both trivial order and featureless randomness [37]. All cases exhibit complexity values in the range 0.022–0.034, with the two equal-amplitude configuration showing the highest initial complexity ($C_0 = 0.034$) due to the structured interference pattern. The temporal variations appear anticorrelated with spectral entropy: complexity decreases as entropy increases during collision events, consistent with the interpretation that transient spectral broadening reduces the disequilibrium component D while increasing the entropy component H .

Panel (d) presents the Fisher information F , which measures the sharpness or localization of the spatial amplitude distribution according to equation (67). Higher values indicate more localized, sharper-peaked structures. The three-soliton case exhibits the highest mean Fisher information ($0.960 \pm 0.148 \text{ m}^{-2}$), reflecting the presence of multiple narrow peaks, while the two equal-amplitude case shows the lowest ($0.641 \pm 0.119 \text{ m}^{-2}$) due to the broader, lower-amplitude solitons. Notably, the collision case displays pronounced spikes in Fisher information (reaching 1.8 m^{-2}) during the interaction event, reflecting the transient steepening of gradients as the soliton profiles merge. These transient features subsequently relax as the waves separate, consistent with the elastic nature of KdV soliton collisions.

Table 2 summarizes the mean values of the information-theoretic measures across all test cases.

Table 2: Summary of information-theoretic measures (mean \pm standard deviation over simulation time).

Case	S_k	$C (\times 10^{-2})$	$F [\text{m}^{-2}]$
1 (Single soliton)	0.528 ± 0.021	2.55 ± 0.22	0.801 ± 0.180
2 (Two equal)	0.508 ± 0.018	2.99 ± 0.20	0.641 ± 0.119
3 (Collision)	0.567 ± 0.024	2.47 ± 0.22	0.837 ± 0.179
4 (Three solitons)	0.514 ± 0.012	2.49 ± 0.07	0.960 ± 0.148

The complete integrability of the KdV equation implies that phase space trajectories are confined to low-dimensional invariant manifolds [5]. RQA provides tools to characterize this structure without requiring explicit identification of action-angle variables. Figure 6 presents phase space diagnostics for the collision case (Case 3) alongside comparison with the single-soliton reference.

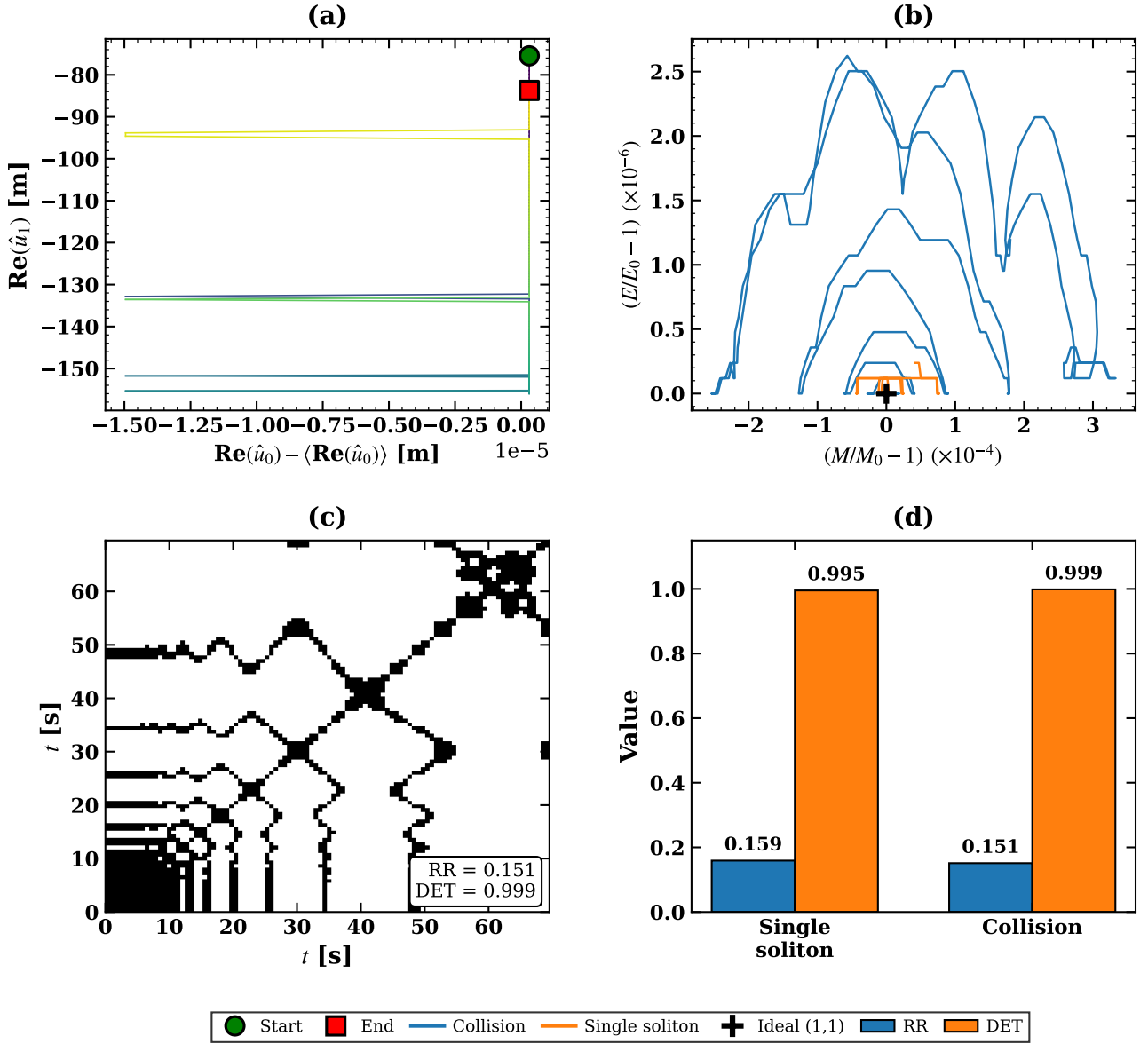


Figure 6: Phase space analysis for the collision case. (a) Trajectory in Fourier mode space (real parts of modes 0 and 1), colored by time; (b) trajectory in normalized conservation space (M/M_0 , E/E_0); (c) recurrence plot with quantification metrics; (d) comparison of recurrence rate (RR) and determinism (DET) between single-soliton and collision cases.

Panel (a) displays the trajectory in a two-dimensional projection of Fourier mode space, plotting the real part of the first mode $\text{Re}(\hat{u}_1)$ against deviations of the zeroth mode $\text{Re}(\hat{u}_0) - \langle \text{Re}(\hat{u}_0) \rangle$. The zeroth mode, proportional to the spatial mean, exhibited negligible variation ($|\hat{u}_0| = 178.85 \pm 0.00$ m), consistent with mass conservation. Higher modes showed larger fluctuations correlated with collision dynamics: $|\hat{u}_1| = 149.9 \pm 16.0$ m and $|\hat{u}_2| = 97.8 \pm 27.2$ m. The trajectory traces a bounded path in this projection, with the color gradient indicating temporal progression from the start (green circle) to end (red square) of the simulation.

Panel (b) presents the trajectory in normalized conservation space, plotting $(M/M_0 - 1)$ against $(E/E_0 - 1)$. The ideal conservative dynamics would confine the trajectory to a single point at the origin. The computed trajectory remains confined to an extremely small region: $M/M_0 \in [0.9997, 1.0003]$ and $E/E_0 \in [1.0000, 1.0000026]$, with total extent approximately 5.86×10^{-4} . The single-soliton case (orange trace) occupies an even smaller region, while both trajectories cluster near the ideal point (black cross), confirming the high fidelity of the numerical conservation.

The recurrence plot in panel (c) visualizes the binary recurrence matrix R_{ij} defined in equation (71), where black pixels indicate times t_i and t_j at which the conservation space trajectory revisits the same neighborhood (within threshold $\varepsilon = 3.52 \times 10^{-5}$). The diagonal line structures indicate deterministic dynamics: when the system visits a particular state, it subsequently follows a trajectory parallel to previous visits, characteristic of regular (non-chaotic) motion on invariant manifolds [41, 42]. The recurrence rate $\text{RR} = 0.151$ indicates that approximately 15% of state pairs satisfy the recurrence criterion, while the determinism $\text{DET} = 0.999$ confirms

that nearly all recurrences form diagonal line structures.

Panel (d) compares the RQA metrics between the single-soliton and collision cases. Both exhibit similar recurrence rates (0.159 and 0.151, respectively) and high determinism (0.995 and 0.999). The marginally higher determinism in the collision case may appear counterintuitive but likely reflects the longer simulation time (70 s versus 50 s) providing more opportunities for trajectory segments to align. A correlation dimension estimate of 0.86 for the collision case, computed from the recurrence matrix scaling [42], suggests that the effective dynamics occupy a manifold of dimension less than unity—consistent with the trajectory being confined near a fixed point (the ideal conservation state) with small bounded oscillations.

4 Discussion

The results presented above demonstrate that the `sangkuriang` solver successfully reproduces the essential features of KdV soliton dynamics while maintaining numerical accuracy appropriate for research applications in idealized ocean wave modeling. Several aspects merit further discussion in the context of GFD and coastal oceanography.

The pseudo-spectral spatial discretization combined with eighth-order adaptive time integration achieved conservation errors ranging from $\mathcal{O}(10^{-7})$ to $\mathcal{O}(10^{-4})$ across the test cases. These values compare favorably with those reported in the literature for similar methods applied to nonlinear dispersive equations arising in ocean wave theory [17, 20]. The observation that momentum and energy are conserved more accurately than mass warrants consideration. The mass functional (30) involves only the solution field itself, making it sensitive to any drift in the solution mean. In contrast, the momentum functional (31) depends on u^2 , which suppresses the contribution of small-amplitude dispersive radiation relative to the dominant soliton peaks. The energy functional (32), involving spatial derivatives, further weights the smooth soliton cores over high-wavenumber numerical artifacts. This hierarchy suggests that the mass error may serve as a conservative upper bound on overall numerical accuracy. From an oceanographic standpoint, the high fidelity of momentum and energy conservation is particularly reassuring, as these quantities govern the transport of wave energy and the forces exerted by solitary waves on offshore structures and the seabed [48].

The absence of systematic drift in the conservation time series indicates that the DOP853 integrator, while not symplectic, introduces primarily oscillatory rather than secular errors for the integration times considered. For significantly longer simulations—such as those required to model solitary wave propagation across an entire continental shelf or ocean basin—the accumulation of these oscillatory errors could potentially become problematic, and structure-preserving integrators [33, 43] might offer advantages despite their typically higher computational cost per step.

The close agreement between measured and theoretical soliton velocities ($< 5\%$ discrepancy) confirms that the computed solutions satisfy the fundamental amplitude–velocity relationship (34). This nonlinear dispersion relation is the same scaling that governs the rank ordering and separation of internal solitary waves observed in the ocean, where larger-amplitude waves consistently propagate faster than their smaller counterparts [46, 49]. The small systematic excess in measured velocities relative to predictions based on mean amplitude may arise from several factors. First, the soliton amplitudes evolve during the initial adjustment phase as the approximate initial conditions relax toward exact soliton profiles, and velocity measurements based on trajectory slopes integrate over this transient. Second, the theoretical velocity assumes an isolated soliton in an infinite domain, whereas the periodic boundary conditions and finite domain introduce corrections that may slightly modify the effective dispersion relation [18]. Similar discrepancies between observed and theoretically predicted propagation speeds have been documented in field studies of oceanic internal solitary waves, where background currents, stratification variability, and bathymetric effects introduce additional corrections to the idealized KdV prediction [47, 50].

The high linearity of all tracked trajectories ($R^2 > 0.99$) provides strong evidence that the computed waves behave as true solitons rather than dispersive wave packets that would spread and decelerate over time. This validation is particularly meaningful for the post-collision segments, where any deviation from integrability would manifest as amplitude-dependent velocity changes. In the oceanic context, the persistence of soliton identity through collisions is a key feature that enables the long-range propagation of internal solitary waves across hundreds of kilometers of continental shelf [46, 51].

The spectral and information-theoretic analyses reveal consistent patterns that reflect the integrable structure of the KdV equation. The bounded variations of spectral entropy, statistical complexity, and Fisher information—with transient excursions during collisions that subsequently relax—indicate that the wave field returns to its pre-collision information content. This behavior contrasts with what would be expected for non-integrable systems, where collision events could transfer energy to radiation modes, leading to secular changes in these measures [6]. In realistic ocean settings, perturbations to perfect integrability arise from variable stratification, background shear, and bathymetric gradients [50]; the diagnostic tools developed here could serve to quantify the degree to which such perturbations disrupt the regular structure of the idealized KdV dynamics.

The Fisher information proved particularly sensitive to collision dynamics, with pronounced spikes corresponding to the transient steepening of gradients during wave merging. This sensitivity suggests that Fisher information may serve as a useful diagnostic for detecting the onset and completion of soliton interactions in more complex scenarios, including the multi-wave interaction events observed in energetic oceanic internal wave environments such as the South China Sea [49] and the Strait of Gibraltar.

The RQA provides independent confirmation of the regular, non-chaotic dynamics expected for an integrable

Hamiltonian system. The high determinism values ($\text{DET} > 0.99$) indicate that the phase space trajectory exhibits the parallel structure characteristic of motion on invariant tori, rather than the mixing behavior associated with chaotic dynamics [42]. The estimated correlation dimension below unity is consistent with the trajectory being confined near a fixed point (the exact conservation state) with small-amplitude oscillations.

These results suggest that RQA could serve as a model-independent diagnostic for assessing the integrability of computed solutions in situations where analytical results are unavailable. Significant deviations from high determinism might indicate either numerical breakdown of integrability due to insufficient resolution, or genuine non-integrable dynamics in perturbed KdV-type equations. This capability is potentially valuable for ocean wave modeling, where extended KdV equations with variable coefficients are routinely employed to account for realistic oceanographic conditions [48, 50], and where the degree to which the integrable structure survives such extensions is not always known a priori.

The demonstration that research-grade KdV simulations can be performed in minutes on a laptop-class workstation represents a practical advantage for exploratory studies in physical oceanography and GFD. The Numba-accelerated implementation achieved throughputs of approximately 1000–1400 time steps per second, suggesting that the solver is not severely memory-bandwidth limited for the grid sizes considered. The observed scaling from $N = 512$ to $N = 1024$ (throughput reduction from ~ 1300 to ~ 1030 steps/s) is consistent with the $\mathcal{O}(N \log N)$ FFT complexity combined with increased cache pressure. The accessibility of this computational tool on commodity hardware lowers the barrier for researchers and graduate students in oceanography to conduct idealized numerical experiments on nonlinear dispersive wave dynamics without requiring institutional high-performance computing allocations.

For applications requiring higher resolution or longer integration times—such as simulating solitary wave propagation over shelf-scale distances or conducting ensemble studies across a range of oceanic stratification profiles—several optimization strategies could be considered: vectorized evaluation of multiple initial conditions in parallel, GPU acceleration of FFT operations via CuPy [44], or time-parallel algorithms for ensemble simulations. The modular architecture of `sangkuriang` is designed to facilitate such extensions while maintaining compatibility with the existing analysis framework.

Several limitations of the present study should be acknowledged. First, the test cases employed approximate sech^2 initial conditions rather than exact N -soliton solutions obtainable from inverse scattering theory [5]; comparison with exact solutions would provide a more stringent validation. Second, the periodic boundary conditions preclude investigation of soliton interactions with boundaries or non-periodic wave backgrounds, which are relevant to realistic coastal settings where waves encounter shorelines, headlands, or river plumes. Third, the standard KdV equation considered here represents only the leading-order balance between nonlinearity and dispersion; extensions to higher-order equations (e.g., the modified KdV or Kawahara equations [45]) and variable-coefficient formulations that account for slowly varying bathymetry and stratification [50] would broaden the solver’s applicability to different oceanic regimes. Fourth, the present study considers only surface wave analogs; the extension to internal wave dynamics in continuously stratified fluids requires the incorporation of modal structure and density-dependent coefficients [46, 48].

Future development of `sangkuriang` could address these limitations while maintaining the design philosophy of accessibility and reproducibility. The integration of inverse scattering routines would enable exact initial conditions for validation studies. Variable-coefficient extensions would permit modeling of wave propagation over varying bathymetry, a critical capability for realistic coastal ocean applications [50, 51]. The incorporation of rotational effects through the Ostrovsky equation would extend applicability to internal waves at scales where the Earth’s rotation becomes significant [47]. Perhaps most significantly, the pseudo-spectral framework could be extended to two-dimensional generalizations such as the Kadomtsev–Petviashvili equation [6], enabling investigation of oblique soliton interactions and transverse instabilities relevant to the three-dimensional propagation patterns of oceanic internal waves observed in satellite imagery [49].

5 Conclusions

We have presented `sangkuriang`, an open-source pseudo-spectral solver for the KdV equation combining Fourier-based spatial discretization with adaptive eighth-order Runge–Kutta time integration. Systematic validation across four test cases of increasing complexity—from isolated soliton propagation to three-body interactions motivated by oceanic internal solitary wave dynamics—confirmed conservation of the KdV invariants to relative errors below 10^{-5} for momentum and energy, while measured soliton velocities agreed with the theoretical amplitude–velocity relation to within 5%. Information-theoretic diagnostics revealed bounded spectral entropy and near-unit phase-space determinism throughout all simulations, providing quantitative evidence that the numerical solutions preserve the integrable Hamiltonian structure of the governing equation. Implemented in Python with Numba-accelerated parallel execution, the solver completed the most demanding configuration—a three-soliton interaction over 80 s at $N = 1024$ resolution—in under ten minutes on a laptop workstation, demonstrating accessibility for researchers in oceanography and GFD without requiring high-performance computing resources.

The idealized test cases examined here—single-soliton propagation, symmetric pairs, overtaking collisions, and rank-ordered three-wave packets—capture the essential nonlinear dispersive dynamics that underpin a wide range of oceanic solitary wave phenomena, from internal soliton trains on continental shelves to long gravity waves in coastal basins. By establishing the fidelity of the `sangkuriang` solver against these canonical benchmarks, the

present work provides a verified computational foundation upon which more realistic ocean wave studies can be built.

Beyond its immediate utility for KdV simulations, the diagnostic framework developed here—combining conservation monitoring, spectral information measures, and recurrence quantification—offers a transferable methodology for assessing integrability preservation in numerical solutions of nonlinear dispersive PDEs arising in GFD. Extensions to variable-coefficient KdV variants relevant to wave propagation over realistic bathymetry, higher-order dispersive equations such as the Kawahara equation, rotational generalizations including the Ostrovsky equation for internal waves influenced by the Earth’s rotation, and two-dimensional formulations such as the Kadomtsev–Petviashvili equation represent natural directions for future development within the existing pseudo-spectral framework. Such extensions would progressively bridge the gap between the idealized dynamics studied here and the full complexity of nonlinear wave propagation in the real ocean.

Author Contributions

Conceptualization, D.E.I. and S.H.S.H.; methodology, D.E.I., S.H.S.H., and F.K.; software, S.H.S.H.; validation, D.E.I., S.H.S.H., and F.K.; formal analysis, S.H.S.H.; investigation, D.E.I. and S.H.S.H.; resources, D.E.I., I.P.A., and R.S.; data curation, S.H.S.H.; writing—original draft preparation, S.H.S.H.; writing—review and editing, D.E.I., A.P., R.D.K., F.K., I.P.A., K.A.S., A.P.H., F.R.F., and R.S.; visualization, S.H.S.H.; supervision, D.E.I., I.P.A., K.A.S., A.P.H., F.R.F., and R.S.; project administration, D.E.I.; funding acquisition, D.E.I., S.H.S.H., F.K., A.P.H., F.R.F., and R.S. All authors have read and agreed to the published version of the manuscript.

Funding

This study was supported by the Program Penelitian, Pengabdian kepada Masyarakat, dan Inovasi FITB 2026, the Dean’s Distinguished Fellowship 2023 from the University of California, Riverside, the Riset Dosen Muda 2025, the Riset Unggulan 2026, and the Riset Talenta Unggul 3P 2026 from Bandung Institute of Technology.

Data Availability

The `sangkuriang` library source code is available on GitHub at <https://github.com/sandyherho/sangkuriang-ideal-solver> under the MIT license and can be installed from PyPI at <https://pypi.org/project/sangkuriang-ideal-solver/>. The Python scripts for data analysis (https://github.com/sandyherho/suppl_sangkuriang) and all simulation outputs—including animations, NetCDF data files, figures, computational logs, and statistical analyses—archived on the Open Science Framework (OSF) (<https://doi.org/10.17605/OSF.IO/MS5EJ>) are released under the MIT license.

Acknowledgments

The authors thank the anonymous reviewers for their constructive comments. During the preparation of this work, the authors used Claude Sonnet 4.5 (Anthropic) to assist with English grammar, vocabulary, and stylistic refinement. All mathematical derivations, numerical methods, scientific analysis, interpretation of results, and intellectual content were produced entirely by the authors. The authors reviewed and edited all AI-assisted outputs and take full responsibility for the content of the publication.

Conflicts of Interest

The authors declare no conflicts of interest. The funders had no role in the design of the study; in the collection, analyses, or interpretation of data; in the writing of the manuscript; or in the decision to publish the results.

Abbreviations

CF	Climate and Forecast
CPU	Central Processing Unit
DFT	Discrete Fourier Transform
DOP853	Dormand–Prince 8(5,3) method
FFT	Fast Fourier Transform
FFTW	Fastest Fourier Transform in the West
GFD	Geophysical Fluid Dynamics
IFFT	Inverse Fast Fourier Transform
ISW	Internal Solitary Wave
JIT	Just-In-Time
KdV	Korteweg–de Vries
LLVM	Low Level Virtual Machine
LMC	López–Ruiz–Mancini–Calbet
MKL	Math Kernel Library
NetCDF	Network Common Data Format
ODE	Ordinary Differential Equation
OpenMP	Open Multi-Processing
PDE	Partial Differential Equation
PyPI	Python Package Index
RMS	Root Mean Square
RQA	Recurrence Quantification Analysis

References

- [1] Drazin, P.G.; Johnson, R.S. *Solitons: An Introduction*, 2nd ed.; Cambridge University Press: Cambridge, UK, 1989.
- [2] Korteweg, D.J.; de Vries, G. On the Change of Form of Long Waves Advancing in a Rectangular Canal, and on a New Type of Long Stationary Waves. *Philos. Mag.* **1895**, *39*, 422–443.
- [3] Zabusky, N.J.; Kruskal, M.D. Interaction of “Solitons” in a Collisionless Plasma and the Recurrence of Initial States. *Phys. Rev. Lett.* **1965**, *15*, 240–243.
- [4] Gardner, C.S.; Greene, J.M.; Kruskal, M.D.; Miura, R.M. Method for Solving the Korteweg-deVries Equation. *Phys. Rev. Lett.* **1967**, *19*, 1095–1097.
- [5] Ablowitz, M.J.; Kaup, D.J.; Newell, A.C.; Segur, H. The Inverse Scattering Transform-Fourier Analysis for Nonlinear Problems. *Stud. Appl. Math.* **1974**, *53*, 249–315.
- [6] Ablowitz, M.J. *Nonlinear Dispersive Waves: Asymptotic Analysis and Solitons*; Cambridge University Press: Cambridge, UK, 2012.
- [7] Whitham, G.B. *Linear and Nonlinear Waves*; John Wiley & Sons: New York, NY, USA, 1999.
- [8] Durran, D.R. *Numerical Methods for Fluid Dynamics: With Applications to Geophysics*; Springer: New York, NY, USA, 2010.
- [9] Herho, S.H.S.; Fajary, F.R.; Herho, K.E.P.; Anwar, I.P.; Suwarman, R.; Irawan, D.E. Reappraising Double Pendulum Dynamics across Multiple Computational Platforms. *CLEI Electron. J.* **2025**, *28*, 10.
- [10] Herho, S.H.S.; Kaban, S.N.; Nugraha, C. OptionMC: A Python Package for Monte Carlo Pricing of European Options. *Int. J. Data Sci.* **2025**, *6*, 70–84.
- [11] Harris, C.R.; Millman, K.J.; van der Walt, S.J.; et al. Array Programming with NumPy. *Nature* **2020**, *585*, 357–362.
- [12] Virtanen, P.; Gommers, R.; Oliphant, T.E.; et al. SciPy 1.0: Fundamental Algorithms for Scientific Computing in Python. *Nat. Methods* **2020**, *17*, 261–272.
- [13] Lam, S.K.; Pitrou, A.; Seibert, S. Numba: A LLVM-Based Python JIT Compiler. In *Proceedings of the Second Workshop on the LLVM Compiler Infrastructure in HPC*; Austin, TX, USA, 15 November 2015; pp. 1–6.
- [14] Herho, S.H.S.; Trilaksono, N.J.; Fajary, F.R.; et al. kh2d-solver: A Python Library for Idealized Two-Dimensional Incompressible Kelvin–Helmholtz Instability. *Appl. Comput. Mech.* **2025**, *19*, 125–156.
- [15] Pavlenko, M.P.; Pavlenko, L.V.; Iotov, Y.V.; Pavlenko, Y.M. Experience in the Development and Implementation of the Course “Python for Physics Teachers”. *J. Phys. Conf. Ser.* **2025**, *3105*, 012011.
- [16] Tufino, E.; Oss, S.; Alemani, M. Integrating Python Data Analysis in an Existing Introductory Laboratory Course. *Eur. J. Phys.* **2024**, *45*, 045707.
- [17] Trefethen, L.N. *Spectral Methods in MATLAB*; SIAM: Philadelphia, PA, USA, 2000.
- [18] Boyd, J.P. *Chebyshev and Fourier Spectral Methods*, 2nd ed.; Dover Publications: Mineola, NY, USA, 2001.
- [19] Canuto, C.; Hussaini, M.Y.; Quarteroni, A.; Zang, T.A. *Spectral Methods: Evolution to Complex Geometries and Applications to Fluid Dynamics*; Springer: Berlin, Germany, 2007.
- [20] Fornberg, B. *A Practical Guide to Pseudospectral Methods*; Cambridge University Press: Cambridge, UK, 2009.
- [21] Dormand, J.R.; Prince, P.J. A Family of Embedded Runge-Kutta Formulae. *J. Comput. Appl. Math.* **1980**,

- 6, 19–26.
- [22] Hairer, E.; Wanner, G.; Nørsett, S.P. *Solving Ordinary Differential Equations I: Nonstiff Problems*, 2nd ed.; Springer: Berlin, Germany, 1993.
- [23] Rew, R.; Davis, G. NetCDF: An Interface for Scientific Data Access. *IEEE Comput. Graph. Appl.* **1990**, *10*, 76–82.
- [24] Dingemans, M.W. *Water Wave Propagation Over Uneven Bottoms: Part 1*; World Scientific: Singapore, 1997.
- [25] Dingemans, M.W. *Water Wave Propagation Over Uneven Bottoms: Part 2*; World Scientific: Singapore, 1997.
- [26] Johnson, R.S. *A Modern Introduction to the Mathematical Theory of Water Waves*; Cambridge University Press: Cambridge, UK, 1997.
- [27] Chiang, C.M. *The Applied Dynamics of Ocean Surface Waves*; World Scientific: Singapore, 1992.
- [28] Miura, R.M. Korteweg-de Vries Equation and Generalizations. I. A Remarkable Explicit Nonlinear Transformation. *J. Math. Phys.* **1968**, *9*, 1202–1204.
- [29] Brigham, E.O. *The Fast Fourier Transform and Its Applications*; Prentice-Hall: Upper Saddle River, NJ, USA, 1988.
- [30] Cooley, J.W.; Tukey, J.W. An Algorithm for the Machine Calculation of Complex Fourier Series. *Math. Comp.* **1965**, *19*, 297–301.
- [31] Gottlieb, D.; Orszag, S.A. *Numerical Analysis of Spectral Methods: Theory and Applications*; SIAM: Philadelphia, PA, USA, 1977.
- [32] Prince, P.J.; Dormand, J.R. High Order Embedded Runge-Kutta Formulae. *J. Comput. Appl. Math.* **1981**, *7*, 67–75.
- [33] Bridges, T.J.; Reich, S. Numerical Methods for Hamiltonian PDEs. *J. Phys. A Math. Gen.* **2006**, *39*, 5287–5320.
- [34] Atkinson, K.E. *An Introduction to Numerical Analysis*, 2nd ed.; John Wiley & Sons: New York, NY, USA, 1991.
- [35] Hunter, J.D. Matplotlib: A 2D Graphics Environment. *Comput. Sci. Eng.* **2007**, *9*, 90–95.
- [36] Shannon, C.E. A Mathematical Theory of Communication. *Bell Syst. Tech. J.* **1948**, *27*, 379–423.
- [37] López-Ruiz, R.; Mancini, H.L.; Calbet, X. A Statistical Measure of Complexity. *Phys. Lett. A* **1995**, *209*, 321–326.
- [38] Fisher, R.A. Theory of Statistical Estimation. *Math. Proc. Camb. Phil. Soc.* **1925**, *22*, 700–725.
- [39] Frieden, B.R. *Science from Fisher Information: A Unification*; Cambridge University Press: Cambridge, UK, 2004.
- [40] Ly, A.; Marsman, M.; Verhagen, J.; Grasman, R.P.P.P.; Wagenmakers, E.-J. A Tutorial on Fisher Information. *J. Math. Psychol.* **2017**, *80*, 40–55.
- [41] Eckmann, J.-P.; Kamphorst, S.O.; Ruelle, D. Recurrence Plots of Dynamical Systems. *Europhys. Lett.* **1987**, *4*, 973–977.
- [42] Marwan, N.; Romano, M.C.; Thiel, M.; Kurths, J. Recurrence Plots for the Analysis of Complex Systems. *Phys. Rep.* **2007**, *438*, 237–329.
- [43] Hairer, E.; Wanner, G.; Lubich, C. *Geometric Numerical Integration: Structure-Preserving Algorithms for Ordinary Differential Equations*, 2nd ed.; Springer: Berlin, Germany, 2006.
- [44] Okuta, R.; Unno, Y.; Nishino, D.; Hido, S.; Loomis, C. CuPy: A NumPy-Compatible Library for NVIDIA GPU Calculations. In *Proceedings of the Workshop on Machine Learning Systems, NIPS*; Long Beach, CA, USA, 8 December 2017.
- [45] Kawahara, T. Oscillatory Solitary Waves in Dispersive Media. *J. Phys. Soc. Jpn.* **1972**, *33*, 260–264.
- [46] Helfrich, K.R.; Melville, W.K. Long Nonlinear Internal Waves. *Annu. Rev. Fluid Mech.* **2006**, *38*, 395–425.
- [47] Grimshaw, R.; Pelinovsky, E.; Talipova, T. The Modified Korteweg–de Vries Equation in the Theory of Large-Amplitude Internal Waves. *Nonlinear Process. Geophys.* **1997**, *4*, 237–250.
- [48] Osborne, A. *Nonlinear Ocean Waves and the Inverse Scattering Transform*; Academic Press: Burlington, MA, USA, 2010.
- [49] Jackson, C.R. *An Atlas of Internal Solitary-like Waves and Their Properties*, 2nd ed.; Global Ocean Associates: Alexandria, VA, USA, 2004.
- [50] Grimshaw, R.; Pelinovsky, E.; Talipova, T.; Kurkina, O. Internal Solitary Waves: Propagation, Deformation and Disintegration. *Nonlinear Process. Geophys.* **2010**, *17*, 633–649.
- [51] Lamb, K.G. Internal Wave Breaking and Dissipation Mechanisms on the Continental Slope/Shelf. *Annu. Rev. Fluid Mech.* **2014**, *46*, 231–254.